Manuscript prepared for Hydrol. Earth Syst. Sci.
with version 5.0 of the LaTeX class copernicus.cls.
Date: 24 July 2014

Hydrometeorological Effects of Historical Land-Conversion in an Ecosystem-Atmosphere Model of Northern South America

Ryan G. Knox[1,5], **Marcos Longo**[2], **Abigail L. S. Swann**[3], **Ke Zhang**[2,6], **Naomi M. Levine**[2], **Paul R. Moorcroft**[2], **and Rafael L. Bras**[4]

[1]Massachusetts Institute of Technology, Cambridge, Massachusetts, USA
[2]Harvard University, Cambridge, Massachusetts, USA
[3]University of Washington, Seattle, Washington, USA
[4]Georgia Institute of Technology, Atlanta, Georgia, USA
[5]now at: Lawrence Berkeley National Laboratory, Berkeley, California, USA
[6]now at: Cooperative Institute for Mesoscale Meteorological Studies, University of Oklahoma, Oklahoma, USA

Correspondence to: Ryan G. Knox
rgknox@lbl.gov

Abstract. This work investigates how the integrated land-use of northern South America has affected the present day (circa 2000) regional patterns of hydrology. A numerical model of the terrestrial ecosystems (Ecosystem Demography Model 2 - ED2) is combined with an atmospheric model (Brazilian Regional Atmospheric Modeling System - BRAMS) to investigate how land conversion in the Amazon and northern South America have changed the hydrology of the region. Two numerical realizations of the structure and composition of terrestrial vegetation are used as boundary conditions that drive the simulation. One realization captures the present day vegetation condition that includes deforestation and land-conversion, the other is an estimate of the potential structure and composition of the region's vegetation without human influence. Model output is assessed for consistent and significant pattern differences in hydrometeorology. Results show that South American land conversion can drive consistent changes to the regional patterning of precipitation. Land-conversion was not associated with a significant bias in continental mean precipitation, but was associated with a negative bias in mean continental evaporation and a positive bias in continental runoff. Two focus areas, one in the Brazilian state of Pará, and one in the Gran Chaco, are selected to scrutinize the basis of differential hydrology and hydrometeorology manifested by the two scenarios. In both cases, deforestation led to increases in total surface albedo, driving decreases in net-radiation, boundary layer moist static energy and ultimately convective precipitation. In the case of the Gran Chaco, decreased precipitation was also a result of decreased advective moisture transport, indicating that differences in local hydrometeorology may manifest via teleconnections with the greater region.

1 Introduction

The literature documenting Amazonian land conversion and surrounding areas is significant, the reader is referred to a small selection of non-exhaustive references for some background, (Cardille and Foley, 2003)(Skole and Tucker, 1993)(INPE, 2003)(Nepstad et al., 2001)(Geist and Lambin, 2002)(Laurance et al., 2001)(Nepstad et al., 2001). The work presented here is motivated by a need to better understand how the history of this significant land-conversion has influenced the hydrology of the region. Seminal studies with General Circulation Models have predicted that massive and widespread Amazonian deforestation would lead to regional reductions in precipitation, evaporation and moisture convergence, with slight increases in surface temperature (Henderson-Sellers et al., 1993)(Nobre et al., 1991)(Lean and Warrilow, 1989)(Dickinson and Henderson-Sellers, 1998). As will be outlined further, the mechanistic relationships between land-conversion and hydrometeorological response is complex and has benefited from study with newer generations of land-atmosphere models with increased granularity and increased complexity in representing physical process. This enables a better understand the sensitivities of the earth system to a specific anthropogenic forc-

ing, which is useful in making better predictions of the earth system and informing land-management practices.

There are several direct hydrologic mechanisms that connect changes in tropical forest structure (i.e. deforested versus intact canopies) to the regional climate system. Stems and leaves absorb light at different magnitudes over the visible and thermal spectrum compared to bare earth and grasses, typically resulting in a lower surface albedo and higher levels of net surface radiation. This directly impacts atmospheric radiative heating/cooling rates and the net flux of sensible and latent heat into the atmosphere. Forest leaf surfaces also increase the interception of precipitation, which influences the land surface water balance and the partition that is redirected toward the atmosphere. Forests typically have higher leaf areas and therefore higher total capacity for transpiration due to higher total stomata density.

Forests with deep rooted trees draw from deeper soil moisture pools, which have different periodicity in available water and therefore alter the timing of latent heat flux via transpiration compared to grasslands(Kleidon and Heimann, 2000)(Nepstad et al., 1994). Below the canopy crown, litterfall and forest floor vegetation combine with leaf interception to enhance overall retention of water from runoff both on the surface and through the soil. Canopy structure also changes the drag surface imposed on the atmospheric boundary layer and the manifestation of shear and in-canopy turbulent transport of heat, moisture and momentum.

The differential effects that forests and non-forests have on surface hydrology, shift the balance of latent and sensible heat flux creating a potential trade-off between the mechanisms that trigger convective initiation and the mechanisms that sustain deep convection(Peilke, 2005)(Wang et al., 2009). Latent heat flux is a potential source of convective available potential energy (CAPE) which is essential for driving deep convection. However, sensible heat flux drives the large thermal motions that stimulate boundary layer growth and are likewise needed to trigger convection (Pielke, 2001).

The higher surface temperatures associated with widespread deforestation, as reported with the first generations of General Circulation models and beyond, (Henderson-Sellers et al., 1993)(Nobre et al., 1991)(Lean and Warrilow, 1989)(Dickinson and Henderson-Sellers, 1998) are thought to be the result of losses in evaporative cooling associated with cleared vegetation. A reduction in atmospheric heating follows a reduction in the heat released by precipitating (condensing) atmospheric water, an assumed consequence of reduced land-atmosphere vapor transport (Eltahir and Bras, 1993). These are two opposing forces to moisture convergence. Positive surface temperature anomalies induce convergent circulations coincident with a decrease in surface pressure. Decreased precipitation heating anomalies reduce tendency towards convergence. While surface temperatures may be higher in deforested areas, there would necessarily be a decrease in total surface energy flux as a direct result of an increased surface albedo (Eltahir, 1996).

The complexity of the Amazonian land-atmosphere feedback system, particularly the nature of secondary feed-backs, supports the need to study this system using more sophisticated numerical modeling with increased granularity. Regional land-atmosphere simulations that can parametrize convective clouds indicate that structured land-conversion scenarios elicit shifts in mean basin precipitation, however less so than traditional coarse scale General Circulation Model studies (Silva et al., 2008). Coherent land surface patterns may strengthen convergence zones on the surface, creating vertical wind triggers to thunderstorms. For instance, Avissar and Werth (2004) introduced that coherent land surface patterns transfer heat, moisture and wave energy to the higher latitudes through thunderstorm activity. Moreover, meso-scale simulations are found to capture key cloud feedback processes which fundamentally alter atmospheric response to land-surface heterogeneities (Medvigy et al., 2011). The meso-scale simulations ability to represent more realistic future land-use scenarios predict an expected redistribution of basin rainfall. For example, western propagating squall-lines from the Atlantic are thought to dissipate over regions of wide-spread deforestation(Silva et al., 2008),(d'Almeida et al., 2007). Significant evidence has also shown that convection can be driven by localized convergent air circulations triggered by land-surface heterogeneities, and that the likelihood and quality of resulting events are both dependent on the scale of heterogeneity and the position relative to disturbed and intact landscapes (Pielke, 2001), (Dalu et al., 1996),(Baldi et al., 2008), (Anthes, 1984),(Knox et al., 2011),(Wang et al., 2009).

In summary, there has been progress in coupled land-atmosphere modeling regarding the feed-backs resulting from regional land conversion, particularly in improved granularity and parametrization of atmospheric physics (such as convection and radiation scattering). However at the land-surface, there exists significant variability in the structure and composition of forest canopies that is obscured by traditional land-surface models (LSMs). Physics-based land surface models have non-linear representations of hydrologic and thermodynamic process. Using average canopy structure to represent a grid-cell, uniform albedo, leaf surface interception, and in-canopy radiation scattering, may yield significantly different grid-cell average mass and energy fluxes to the atmosphere, as compared to a model that partitions these physical processes into various discrete canopy structures.

This research uses the Brazilian Regional Atmospheric Modeling System (BRAMS, a variant of the Regional Atmospheric Modeling System (RAMS) (Cotton et al., 2003)) coupled with the Ecosystem Demography Model 2 (ED2 or EDM2, (Moorcroft et al., 2001), (Medvigy et al., 2009)), to explore the sensitivity of hydrologic climate of northern South America in response to present day land conversion. This modeling system can explicitly represent physics

of the canopy and soil system, with sub-grid variability along ecosystem age-structured and vegetation size-structured axes. An experiment is conducted by comparing simulations that singularly differ in their representation of regional vegetation cover, one which captures the present day vegetation condition that includes deforestation and land-conversion, the other being an estimate of the potential structure and composition of the region's vegetation without human influence. Section 2 of this manuscript will detail experiment design of the coupled model experiment. The model system and experiment design is verified by comparison of model output with observations, see Appendices A2, A3, A4, A5 and A6.

In section 3 we evaluate hydrometeorological response to the changes in land-use history in a regional context. In section 4 we evaluate the processes underlying the observed changes in hydrometeorology in two focus areas. A discussion and conclusion of the results follows.

2 Experiment Design

The main task of this experiment is to conduct two regional simulations of the South American biosphere and atmosphere. The defining difference between the two simulations is how the land-surface model (ED2) represents the structure (the distribution of plant sizes) and composition (the distribution of plant types) of the region's terrestrial ecosystems, as a consequence of two different disturbance regimes. In one simulation, the vegetation reflects a structure and composition that has no effects of human land-use, i.e. a *Potential Vegetation* (PV) condition. In the other simulation, the model will incorporate an estimate of modern (e.g. 2008) human land-use, i.e. an *Actual Vegetation* (AV) condition. The procedure is broken down into steps and elaborated upon.

2.1 Description of the Vegetation Model - ED2

The Ecosystem Demography Model 2 predicts the changes in terrestrial vegetation structure, as modulated by the physically based conservation of water, carbon and enthalpy. Its central design philosophy assumes that the stochastic representation of plant communities integrated over a large sample can be portrayed deterministically as land fractions and plant groups, with explicit size (of the plants) and age (time since a patch of soil housing the plants has experienced major disturbance) structure. By discretely representing the distribution of plant sizes and types it can estimate vertical canopy structure, which directly impacts radiation scattering, throughfall interception, and in-canopy transport of scalars. By discretely representing variable disturbance history, the model can also explicitly simulate energy balance over a wide array of canopy types (closed canopies, recovering forests, grasslands, etc.) that exist within the footprint of driving meteorological data. In this experiment, the ED2 model resolves 5 different relevant tropical plant functional types (PFT); C4 grasses, early-successional trees, mid-successional trees, late-successional trees and tropical c2 grasses. In the ED2 system, PFTs are used as sets of attributes that can be applied to numerous explicitly resolved plant groups of different size and in different parts of the disturbance strata.

2.2 Generation of Surface Boundary Conditions

The creation of the vegetation initial conditions use a "spin-up" process. The spin-up process is an off-line dynamic ED2 simulation, where the driving atmospheric information does not come from a coupled atmospheric model but from a pre-compiled data set. The vegetation is initialized with an equal assortment of newly recruited (saplings) plant types. The off-line model is integrated over several centuries by sampling from the climate data set as the vegetation reaches a quasi-equilibrium of climax communities and communities recovering from natural disturbance.

The model soil textures were derived from a combination of databases, this includes (Quesada et al., 2011) within the Amazon basin and a combination of RADAMBRASIL and IGBP-DIS beyond the basin boundaries (Scholes et al., 1995)(Rossato, 2001). The climate data used to drive the spin-up process was derived from the UCAR DS314 product (Sheffield et al., 2006)[1]. The DS314 is based on the National Center for Environmental Prediction's Reanalysis Product (NCEP) and maintains the same global and temporal coverage period but has bias corrections and increased resolution based on assimilation of composite data sets. The DS314 surface precipitation record was further processed such that grid cell average precipitation was downscaled to reflect the point-scale statistical qualities of local rain-gages. This technique used methods of Lammering and Dwyer (Lammering and Dwyer, 2000), and is explained in more detail in (Knox, 2012). The native NCEP reanalysis and European Center for Medium Range Weather Forecasting (ECMWF) 40 year Reanalysis (ERA-40) were also tested as driver data sets. The downscaled DS314 was ultimately chosen due to better agreement of estimated equilibrium biomass with observations (not shown). The comparison of the model initial condition with regional biomass measurements is discussed more in Appendix A2.

Modified DS314 data from 1970-2005 was repeatedly looped to create a 508 year climate. A summary of the simulation conditions in the spin-up is covered in Table 01. The ED2 vegetation structure and composition at the end of the multi-century simulation was saved as the *Potential Vegetation* (PV) initial condition. The *Actual Vegetation* (AV) was

[1]Original data sets used in the DS314 are from the Research Data Archive (RDA) which is maintained by the Computational and Information Systems Laboratory (CISL) at the National Center for Atmospheric Research (NCAR). The original Sheffield/DS314 data are available from the RDA (http://dss.ucar.edu) in data set number ds314.0.

created by continuing the simulation that produced the *Potential Vegetation*, and assumed that the starting year was 1900. This simulation was continued for another 108 years (until 2008) while incorporating human driven land-use change.

The model applies human land-use by reading an externally compiled data set of *land-use transition matrices* (Albani et al., 2006) that defines the area fractions of which various land-covers types will change to another type over the course of the year. Two external data sets are used to create the land-use transition matrices, the Global Land-Use data set (GLU) (Hurtt et al., 2006) and the SIMAMAZONIA-1 data set (Soares-Filho and co authors, 2006). The GLU data set incorporates the SAGE-HYDE 3.3.1 data set and provides land-use transitions in its native format globally, on a 1-degree grid from the years 1700-1999[2]. The SIMAMAZONIA 1 product provides a more intensive assessment of forest cover and deforestation focused in the Amazon basin, starting in the year 2000. The data is formatted as yearly 1-kilometer forest cover grids (forest,non-forest,natural grasslands), of which yearly transition matrices can be calculated by counting and tallying differences in the classes from year to year. The transitions from the GLU data set from 1990-1999 were linearly scaled to have continuity with the SIMAMAZONIA data set that is introduced in 2000. Land-use that occurred prior to 1900 were lumped into a single combined transition applied at the start. A map of the fraction of the land surface containing human land-use is provided, see Figure 01.

Regional maps of above ground biomass for the *Potential Vegetation* (PV) scenario and the differences between the two scenarios (*Actual Vegetation-Potential Vegetation*, or AV-PV) are provided in Figure 02. The majority of above ground biomass in the *Potential* simulation is concentrated in the Amazon basin and the Atlantic Forest of southern Brazil. Late successional broad-leaf evergreens comprise most of the above ground biomass in these regions. Early successional broad-leaf evergreens are a prevalent but secondary contributor to biomass in the Amazon basin. The early successionals contribute the majority of biomass in Cerrado (savanna like ecosystem, mixed open canopy forests with grasses) ecotones found roughly in Central Brazil on the southern border of the Amazon rain-forest. This is consistent with their competition and resource niche which emphasizes fast growth and colonization of disturbed areas (such as fire and drought prone Cerrado). Human land-use is concentrated in the Arc of Deforestation, which is the southern and eastern edge of the Amazon's tropical forests accessible by highways and heavy equipment. Human land-use encapsulated by the GLU data sets has significantly degraded the Atlantic Forest.

[2]The use of the SAGE-HYDE 3.3.1 Global Land-use Data set acknowledges the University of New Hampshire, EOS-WEBSTER Earth Science Information Partner (ESIP) as the data distributor for this data set.

The model estimated equilibrium above ground biomass (AGB) and basal area (BA) that represent the initial condition are compared with a collection of census measurements in (Baker et al., 2004a)(Baker et al., 2004b), see Appendix A2.

2.3 Land-Atmosphere Coupled Simulations

The two coupled land-atmosphere simulations were conducted over four years, from January 2002 through December 2005. These four years were chosen because of the availability of lateral boundary conditions and validation data sets. With the exception of differing vegetation structure at the lower boundary, the lateral boundary conditions, model parameters, initialization of the atmospheric state, and timing are all identical between the two. The lateral boundary conditions (air temperature, specific humidity, geopotential, meridional wind speed, zonal wind-speed) are taken from the European Centre for Medium Range Weather Forecasting's Interim Reanalysis (ERA-Interim) product (Dee and co authors, 2011). The data is interpolated from the ERA-Interim's model native Reduced Gaussian Grid (N128, which has an equatorial horizontal resolution of 0.75^o).

A group of modeling parameters associated with convective parametrization and the radiation scattering of convective clouds were tuned using a manual binary search procedure. The parameters of mean cloud radius, mean cloud depth, cumulus convective trigger mechanism, dynamic control method and the condensate to precipitation conversion efficiency were calibrated against the Tropical Rainfall Measurement Mission 3B43 product and the surface radiation from the Global Energy and Water Cycle Experiment - Surface Radiation Budget product. Fitness metrics include monthly mean spatial bias, mean squared error and the variance ratios (i.e. the spatial variance of mean model output over the spatial variance of the observations). Manual binary search calibration was chosen because of the complexity of the parameter space, the need for human supervision and sanity checks, and the significant computation requirements for each simulation. Fifty four iterations were performed, utilizing a reduced domain in the first group of iterations to facilitate a more rapid calibration. A table of the finalized coupled model run-time conditions is provided in Table 02. Model output was then compared with observations of atmospheric thermodynamic variables, mean regional surface fluxes (precipitation, radiation, latent heat flux and sensible heat flux) and mean cloud cover profiles; these comparisons are provided in Appendices A3, A4, A5 and A6 respectively.

3 Regional Analysis of the Actual and Potential Scenarios

The following analysis of results will repeatedly refer to "differentials", here defined as the subtractive differences of the

Potential vegetation scenario model output from the *Actual* vegetation scenario model output (or alternatively, AV-PV).

3.1 Emergence of Patterning and Continental Biases

The two simulations showed some pattern differences in mean annual precipitation, see Figure 03. Most notably is the emergence of dipole structures in the differential precipitation. The first dipole shows a positive lobe (more *Actual* scenario precipitation) in the North and West of the Amazon Delta and negative in the South and East of the Amazon delta region. Pattern differences also appear on the Peruvian-Bolivian border, although whether or not it can be considered a dipole is left to the reader. In each year, differential precipitation shows increases on the foothills of the Andes Mountains in southern Peru and the northern tip of Bolivia. There is also a decrease in differential precipitation in southern and central Bolivia. However, in each year there is also noise among the pattern. For instance in 2002, 2003 and 2005 there is also a sliver of space in southern Bolivia that shows increases in differential precipitation adjacent to the area of decrease.

A negatively correlated pattern was evident in down-welling short-wave surface radiation (not shown), the response is strongly influenced by increased cloud optical depth where convective precipitation has increased, and vice-versa. The atmospheric model did not incorporate dynamics of atmospheric gases other than multi-phase water, which therefore explain the variability and differences seen in optical depth. Maximum mean annual differences in surface irradiance peak at about $10\ \mathrm{W\,m^{-2}}$, and are strongest over the dipole associated with the precipitation differential, as well as over the eastern Brazilian dry lands (41^oW).

The differential maps indicate distinct and consistent pattern differences in regional precipitation, but less evidence of an overall continental bias in accumulated precipitation. The mean annual continental bias in accumulated precipitation, evapotranspiration and total runoff is presented in Figure 04. A decrease in total continental evapotranspiration and increased runoff associated with human land-conversion was both consistent and more significant from year to year.

Consistent patterning in differential evapotranspiration and transpiration were also evident, see Figure 05. There is a negative bias (associated with *Actual* vegetation) in both transpiration and total evapotranspiration associated with the "arc of Amazonian deforestation" (starting at 48^oW2^oS going clockwise to 62^oW10^oS, also see forest biomass differentials in Figure 02). While there is a clear physical connection between deforestation and hydrologic response to precipitation, a significant portion of the variability in differential evapotranspiration cannot be explained purely by canopy structure and above ground biomass (the correlation of mean annual differentials: $R^2 = 0.4$). Second order effects and complex system feed-backs account for a significant portion of the variability. These effects include differential precipitation, and potentially the effects of differential surface heating and turbulent transport of scalars (heat and water).

3.2 Significance in Hydrologic Differentials and Ecosystem Response

The availability of root-zone soil moisture, photosynthetically active radiation (PAR) and nutrients are examples of resource limitations that can potentially mediate the response of vegetation to changes in climate. Light and water are critical limiters of plant growth, disturbance (particularly through fire), and mortality (which can be functionally related to growth). However the significance of these limiters in how they may drive ecosystem response is dependent on various factors other than the mean, such as the consistency of change (inter-annual variance), when the changes occur (seasonality) and how large the differences are relative to the total. A standard score "ζ" is one way to evaluate consistency, calculated as the inter-annual mean difference (denoted by brackets "<>") divided by the first standard deviation of the normalized difference η of variable x for year t (mean annual precipitation or down-welling shortwave radiation).

$$\eta_{(t)} = \frac{x_{AV,(t)} - x_{PV,(t)}}{0.5\left(x_{AV,(t)} + x_{PV,(t)}\right)} \tag{1}$$

$$\zeta = \frac{\langle \eta \rangle}{\sigma_\eta} \tag{2}$$

The spatial maps of the standard scores for differential precipitation and shortwave radiation are provided in the upper panels of Figure 06. For reference, a standard difference of 1 suggests that the normalized difference is equal to its inter-annual standard deviation. The maps indicate that the differences in precipitation and radiation from the two scenarios are relatively consistent at the two locations previously identified (Pará Brazil and northern Bolivia). They also indicate that the negative precipitation differential, and the positive radiation differential over the regions of intense deforestation (i.e. the Arc of Deforestation) are consistent.

The susceptibility of ecosystems to significant differential precipitation forcing may be derived from an ED2 model mechanic called the "moisture stress index" msi. This metric is simply the fraction of time that ED2 vegetation cohorts (plants) are actively keeping their stomata closed due to water limitations. For an ecosystem with N plant groups (also known as cohorts) indexed i, the mean land-surface moisture stress index is calculated by the leaf area index LAI weighting of the open-fraction f'_o of stomata for each plant group in the community. Brackets "<>" denote an averaging in space and time. The stomatal open fraction f'_o, is based on the ratio of the plant's $demand$ for root zone soil moisture, and the $supply$ of water the roots are capable of extracting at that time. The demand requirement is driven by the max-

imum transpiration the plant would generate given the existing light, carbon and vapor pressure conditions with unlimited soil moisture.

$$\text{msi} = 1 - \langle \frac{\sum_{i=1}^{N} LAI_{(i)} f'_{o(i)}}{\sum_{i=1}^{N} LAI_{(i)}} \rangle \quad (3)$$

$$f'_{o(i)} = \frac{1}{1 + \frac{Demand}{Supply}} \quad (4)$$

Vegetation communities that have experienced high moisture stress indices in the past are more likely to respond structurally to significant changes in precipitation, because subsequent changes in soil moisture availability will have immediate impacts on photosynthesis and the assimilation of carbon. The lower left panel of Figure 06 shows the mean moisture stress index for the *actual* vegetation scenario. The lower right panel of Figure 06 shows a map of above ground biomass as a reference to the extents of the modeled Amazon tropical forests. Note that in the interior of the Amazon basin, moisture stress has little to no influence on stomatal regulation (and subsequently photosynthesis and growth).

4 Hydrometeorological Focus Areas - Pará Brazil and the Gran Chaco

Two locations that coincide with the pattern differences in precipitation are highlighted in Figure 06. Each location shows decreases in normalized precipitation and increases in down-welling short-wave radiation associated with the *Actual Vegetation* scenario. The vegetation of these locations also show a degree of seasonal moisture stress according to the MSI metric presented in section 3.2. One site is centered on $4.5^oS\ 50.5^oW$ in the Brazilian state of Pará. The other site is centered on $19.5^oS\ 63.5^oW$ in the northwestern part of the Bolivian Gran Chaco where it meets the Andes mountains (sometimes referred to as the Montane Gran Chaco). These two locations are chosen as areas of focused evaluation of hydrology and hydrometeorology. For simplicity, these will be referred to as the *Pará* and *Gran Chaco* focus areas.

A representation of the vegetation demographics at the centroids of the two focus areas, as estimated by the ED2 model, are provided in Figure 07. The natural landscapes at the Pará focus areas are dominated by tropical evergreen forests, and are close to (but not within) the ecotone transition between tropical forests and Cerrado. The offline model spin-up of the *Actual* vegetation scenario imposed pastures on approximately $1/3$ of the land-cover. Roughly 10% of the landscape contains old-growth forests that have gone 200 years since the last disturbance. The focus area in the Gran Chaco is located in a region influenced by the outlet of the South American Low Level Jet. The continental precipitation recycling ratio in this area is relatively high compared to the rest of the continent (Eltahir and Bras, 1994). This exact location in the Gran Chaco is a dry forest ecosystem that borders adjacent ecotones of tropical rainforests to the north, montane ecosystems to the west and grasslands to the south. The ED2 model estimated a *Potential* vegetation demographic that is fairly consistent with the depiction of dry forests, a sparse cover of short trees with grasses in the understory. The *Actual* vegetation simulation of the Gran Chaco, driven by the GLU data set (Hurtt et al., 2006), forced 25% of the natural landscape to pasture (grasses), with an accompanying 20% of abandoned and degraded lands. Human land-use at this specific location promoted a complete collapse of the ED2 estimated tree cover, which includes natural landscapes. This specific site is undoubtedly a more aggressive representation of the differences between the *Actual* and *Potential* scenario ecosystems in this region. Human land-conversion has not lead to a collapse of the Gran Chaco's dry-forest ecosystems for the region as a whole.

4.1 Canopy Water and Energy Balance - Pará

Simulated annual precipitation at the Pará focus area was typically around 1500 millimeters per year, the surface energy flux was dominated leaf evaporation and transpiration. Transpiration dominated vapor flux in the dry season (May-November). Runoff in the form of drainage through the lower soil column occurred mostly during the wet season. The time series water and energy balance at the land-surface is summarized in Figure 08. Accumulated water fluxes from the *Potential* vegetation scenario is provided in the upper left panel (A), differential accumulations are provided in the upper right panel (B).

The *Actual* vegetation scenario experienced roughly 10% less surface precipitation at the Pará focus area. However, the site experienced a small net increase ($30mmyr^{-1}$) in precipitation through-fall, due to a proportionally stronger decrease in leaf interception surfaces (see lower left panel of Figure 08). There is also increased drainage in the *actual* vegetation scenario, which appears symptomatic of both increased throughfall and the relatively significant decrease in the root-zone soil moisture sink from transpiration.

The *Actual* vegetation scenario receives more total short-wave and long-wave radiation $(R_{SD} + R_{LD})$, which is directly attributable to the decrease in mean convective cloud albedo associated with the decrease in convective rainfall at the site. Although the site receives more total incoming radiation in the *Actual* vegetation simulation, the surface albedo decreases with the conversion of forests to pasture. This results in more reflected radiation and a decrease in combined sensible and latent heat flux $(H + L)$, see the bottom right panel (D) of Figure 08.

4.2 Canopy Water and Energy Balance - Gran Chaco

The annual precipitation at Gran Chaco in the *Potential* simulation ranged from 500 to nearly 1000 millimeters. Annual precipitation was roughly 15% lower in the *Actual* vegetation simulation. A summary of the differential hydrology is shown in Figure 09. Like the Pará site, land-conversion drove a significant decrease in leaf area, and therefore a significnat decrease in leaf interception of precipitation in the *Actual* (AV) simulation. However in this case, the relative decrease in interception surfaces due to deforestation was less significant than the decrease in total precipitation due to land-atmosphere feedbacks. Therefore, the *Actual* vegetation simulation experienced a *Decrease* in total precipitation throughfall. Soil evaporation acounted for half of the water losses, while leaf and soil evaporation equally combined to represent the other half. The relatively low preciptation rates promoted almost no detectable runoff. Tranpsiration decreased by 20% in the *Actual* simulation, which is a direct consequence of decreased stomatal density and precipitation throughfall.

Notwithstanding the decreased precipitation throughfall in the *Actual* simulation, surface evaporation unexpectedly increased. Despite decreased precipitation through-fall, upper soil column moisture from rain events has a longer residence time in the root zone, as shown in Figure 010. This is an effect of decreased transpiration, and thus moisture in the grass root zone lasts comparatively longer into the dry season. Note that the relative reduction in precipitation throughfall nearly balanced the reduction in transpiration. There is little evidence to suggest that increased soil evaporation rates would maintain indefinately in the *Actual* scenario, which could alternatively be associated with transient changes in soil column storage.

Like the Pará site, land-conversion at Gran Chaco also drove an increase in total surface albedo, a direct effect due to the loss of dark foliage. More incident radiation is reflected which reduces net-radiation. Unlike the Pará focus area, the albedo effect is stronger than the increase in incident radiation, which leads to decreased sensible heat flux (see Figure 09) and slightly cooler annual surface temperatures (not shown).

4.3 Land-Atmosphere Coupling - Pará

Due to the convective nature of dry season precipitation at the Pará site, a hypothesis is made that differential precipitation response is driven by differential surface energy fluxes associated with the land-conversion. A focused evaluation of the atmosphere during a month experiencing significant differential response may elucidate these differences. A box is constructed around this site for the month of September 2003, it contains the extents of the pattern differential precipitation depression, see Figure 011. Table 03 shows a selection of spatio-temporal mean indicators from the bounded domain. To summarize the differences in surface fluxes, the results are consistent with the single site time-series analysis, where the *Actual* vegetation scenario experienced a decrease in net-radiation ($-10\ \mathrm{W\,m^{-2}}$, despite increased incident shortwave radiation) and increased mean surface albedo.

The decreased precipitation and surface energy flux of the *Actual* scenario are accompanied by a boundary layer with lower equivalent potential temperature, see Figure 012. The decrease in boundary layer equivalent potential temperature has a strong physical connection to explaining the decrease in precipitation, particuarly since the vast majority of the precipitation was generated through the convective parameterization (data not shown). This was verified by recording a log of failures in deep convection (precipitating convective clouds) generated by the convective parameterization. All of the bias in these convective failures occuring in the *Actual* simulation was attributed to the generation of convection that resulted in clouds that were too thin to be classified as precipitating deep convection clouds. This is indicative of the how much convective available potential energy (CAPE) can be released through convective bouyancy, which is controlled by the moist static energy in the surface parcels as well as the moist static energy of the mean atmosphere over the depth of the troposphere. Alternatively, there was no positive bias in the logs associated with the inability to trigger parcel bouyancey.

It is questioned if the driving force behind the weakened moist static (equivalent potential temperature profiles) of the *Actual* scenario is solely the result of local surface fluxes or caused by changes in the regional energy circulation. Both scenarios net a negative moisture convergence (divergent) budget for the month (total integrated water mass flux through the box boundaries, normalized by the box area). The *Potential* vegetation scenario loses more water ($-51.32\ \mathrm{kg\,m^{-2}}$) through its lateral boundaries than the AV scenario ($-37.14\ \mathrm{kg\,m^{-2}}$), see Table 03. This can be visualized by flux vectors as well, see Figure 013. In the *Potential* vegetation case shown in left panel, the flow vectors run east-to-west and up-gradient, which means the advecting air mass is gaining moisture and is consistent with the net water divergence described in Table 03.

4.4 Land-Atmosphere Coupling - Gran Chaco

Similar to the case study in Pará, a bounding box was constructed around the Gran Chaco site in April 2003 that captures the pattern differential precipitation depression. The boundaries are shown in black against seasonal precipitation, evapotranspiration and their differentials in Figure 014. Mean statistics are shown in Table 04. The *Actual* scenario experienced less than half as much precipitation ($41\ \mathrm{kg\,m^{-2}}$ compared to $85\ \mathrm{kg\,m^{-2}}$). Differential evaporation between the two scenarios was not as extreme ($111\ \mathrm{kg\,m^{-2}}$ in the *Potential* scenario compared to $83\ \mathrm{kg\,m^{-2}}$ for *Actual*).

The surface energy flux conditions associated convection also told a similar story as in Pará. The *Actual* vegetation scenario experienced more downwelling shortwave radiation yet less net surface radiation, which was influenced by an increased surface albedo. Like the Pará case, the *Actual* scenario experienced a lower equivalent potential temperature over the boundary layer, see Figure 015. The convective parameterization logs accounted that the *Actual* scenario experienced significantly more failed convective events associated with an inability to generate deep clouds (the same reason as the Pará case). Note that the model's cloud depth parameterization is controlled by convective available potential energy. However in this case, about 25% of the bias in failures was also explained by an inability to trigger convection. This is interesting because this case was slightly different from the Pará in that the *Actual* scenario did not experience significantly higher levels of turbulent kinetic energy over the boundary layer.

An analysis of moisture convergence and advective flux was used to better understand the local versus regional controls that drive convective precipitation. Both scenarios showed negative moisture convergence, typical during the onset of the dry season in this region, refer to Table 04. The *Potential* scenario showed significantly less moisture divergence ($-37\ \mathrm{kg\,m^{-2}}$) than the *Actual* scenario ($-52\ \mathrm{kg\,m^{-2}}$). The moisture advected into this region comes via Northerly winds from the moist Amazonian air mass, see the left panel of Figure 016. Moisture transport from the north decreases significantly in the *Actual* scenario, see the right panel of Figure 016.

5 Discussion

5.1 Secondary Forests and Evapotranspiration Patterning

The maps of differential evapotranspiration showed pattern similarity with differential above ground biomass, as compared to a lack of pattern similarity between differential precipitation and above ground biomass. The stronger correlation in differential evapotranspiration and forest biomass is likely due to their direct physical connection. Deforestation directly decreases leaf interception of precipitation. Precipitation that is intercepted by the canopy is more likely to be re-evaporated, as precipitation through-fall has the potential outcome of infiltration and runoff. Secondly, the total transpiration of a landscape is strongly influenced by stomatal density and leaf area, both of which are reduced with land-conversion and deforestation.

However this explanation of process only considers the immediate structural effects of deforestation, which is not static but also has phases of recovery when left un-managed. During the recovery cycle of tropical forests following *natural* disturbance, successfull new growth in the canopy is typically dominated by pioneer species. Pioneer species have lower wood density, higher maximum photosynthetic capacity and quicker vertical growth than late successional species (Laurance et al., 2004),(Poorter et al., 2006),(Chave et al., 2006). Moreover, the period following a disturbance, in which the population is skewed from a climax distribution is significant. The canopy leaf area may flush to previous levels within a century, yet it may take several centuries for total forest biomass to rebound (which can take multiple centuries). This was verified by observing the model spin-up. It is also known that the tree age demographic in the Amazon contains individuals over 1000 years old (Chambers et al., 1998).

The results presented here support that secondary forests undergoing recovery from deforestation can drive detectable pattern increases in total transpired water across the region. It is rationalized that at these locations, there is significant photosynthetic capacity in the form of leaf area, as well as a distribution of members skewed towards rapid growth and high photosynthetic capacity. If there is sufficient available soil water there would be an expected increase in total transpiration. In the *Actual* model scenario containing deforestation effects, the model estimated an increase in early successional tropical evergreens (pioneers) in the recovering forests of northern Pará and Eastern Amazonas (centered on 5S 58W), see Figure 02 second row right panel. There is an increase in regional transpiration here (Figure 05) that has a strong pattern match with the increase in early successional biomass, moreover there is little evidence of influence from pattern precipitation here (see Figure 03).

5.2 Regional Surface Water Balance and Runoff Generation

There was a clear and consistent bias in the total annual evapotranspiration (negative) and runoff (positive) estimated in the *Actual* scenario when integrated over the entire domain of Northern South America. There is some rudimentary explanation of the first order biases in evapotranspiration explained above. The regional runoff bias appears to have several potential explanations and remaining questions. It is clear that in the *Actual* scenario, decreased canopy interception promotes a first order effect of increased canopy

throughfall. However we saw in comparing the Pará and Gran Chaco case studies, that changes in canopy interception can be offset by changes in incident precipitation. Therefore weakened canopy throughfall from deforestation is not ubiquitously associated with regional increases runoff. In a regional water balance analysis, (d'Almeida et al., 2007) also observed wide-spread regional deforestation promoted decreased evapotranspiration and increased runoff. Similar to this study, they also found that precipitation feedback response to deforestation had the potential to impact the water cycling on par with direct effects of surface hydrologic parameters (although in there results, bi-directionally weakening or strengthening the water-cycle depending on heteogeneity and land-cover fractionation).

The increased continental runoff from the *Actual* scenario is driven by higher equilibrium soil moisture. The regional mean soil moisture depth simulated in the *Actual* scenario oscilated around a inter-seasonal mean of 1.40 meters (over an 8 meter medium), averaging 5 centimeters greater than the *Potential* case. As increased runoff has a negative feedback on increased soil water, and there was no significant consistent bias in precipitation, it is most likely that the positive shift in equilibrium soil moisture in the *Actual* scenario is driven by the decreases in regional evapotranspiration.

This experiment highlighted the use of relatively sophisticated vegetation biophysical processes, which incoporated variable vegetation structure, composition, rooting depth and uptake. However the modeling framework did not incorporate lateral transport of any surface moisture. Therefore, these results must be interpreted with the understanding that lateral re-infiltration, lateral vados zone flow, interflow and water table dynamics could not influence soil moisture dynamics. In light of this, this experiment provides a gauge on the strength of the control that evaporation response to deforestation can have on regional water balance and runoff generation. There has been some evidence that soil hydrologic properties can be significantly affected by land-conversion in the tropics, (Zimmermann et al., 2006) found that both infiltrability and upper root-zone saturated hydraulic conductivity was higherst in intact rainforest compared to pasture and tree plantations. Decreased infiltration in pastures has been related to increased runoff generation as well (Munoz-Villers and McDonnell, 2013). But there seems less certainty in the literature in quantifying the evaporation soil-moisture response to regional Amazonian deforestation.

5.3 Intersection of Seasonal Hydrology and Biodiversity on Canopy Process

The two case studies showed that the structure of the vegetation canopy can influence the seasonal cycle of moisture storage and land-atmosphere moisture flux. At the Gran Chaco site, transpiration was greater in the *Potential* vegetation scenario during the wet season when the deeper roots and higher stomatal density of the open canopy forest could access available soil moisture. Alternatively, total evapotranspiration was greater in the *Actual* vegetation scenario at the onset of the dry-season, due mostly to the fact that the grasslands had more available water stored in the upper root-zone, recall Figure 010.

The natural vegetation at the Gran Chaco site is represented "in-model" with early successional broad-leaf evergreen plant functional types, with accompanying C4 grasses. While the demographic size and composition structure, as well as the openness of the canopy shows some similarity with dry-forest structure, it must be realized that the wider range of water conservation strategies observed in nature could influence how the differences in surface to atmosphere energy fluxes play out at this site.

These findings suggest that the next generations of earth system models may benefit from improvements in representing plant diversity. The seasonal flux of surface to atmosphere water vapor is regulated by plants, and can potentially impact the hydrometeorological dynamic of the region. Total evapotranspiration during the transition from the late wet season to early dry season (April) at the Gran Chaco site was significantly larger in the potential vegetation scenario. As shown in box hydrometeorological analysis in Section 4.4, this was a time in the seasonal cycle that also exhibited significantly different instability profiles in the atmosphere, albeit from competing local and regionaly driven mechanisms.

5.4 Drivers of Differential Convective Precipitation

The *Actual* scenario negative precipitation bias at the two focus areas were both accompanied by reductions in net radiation, decreased annual latent heat flux (evapotranspiration) and increased albedo. They also experienced boundary layers with lower mean equivalent potential temperature, which was then related to fewer cumulus events that lacked sufficient convective available potential energy to generate deep clouds (diagnosed through convective logs). Thus the strongest causal link with differential convective precipitation is differing convective available potential energy.

Positive anomolies in sensible heat flux have been linked to boundary layer formation and turbulent kinetic energy, which are thought to promote the triggering of convection. The case study at Pará did show increased boundary layer turbulent kinetic energy and sensible heat flux, and it is possible that increased boundary layer turbulence may had helped recoup some losses in precipitation. This is deductive reasoning however, following that the Gran Chaco case study did not have increased turbulent kinetic energy associated with the *Actual* scenario and it did experience more failed convective events associated with the inability to overcome convective inhibition (where there was no such trend at Pará).

The two case studies offer different evidence as to how local versus regional controls mediated the differences in precipitation. The Pará case study suggests that the negative precipitation differential is driven primarily by changes in the

local surface energy flux. The dry season prevailing winds at Pará flowed *up* the moisture gradient (i.e. gaining moisture not losing moisture). And according to the flux vectors in Figure 013, despite the decreased precipitation of *Actual* scenario the prevailing winds fluxed more moisture into the domain than the *Potential* case. The Gran Chaco case study showed evidence that differential precipitation was responding to a change in the regional circulation as well as changes in the local surface energy fluxes. The prevailing winds came out of the north and flowed *down* the moisture gradient (i.e. losing moisture). While the domain was a net source of moisture (divergent) the net flux into the domain via advection was positive. And the *Actual* scenario experienced a relative decrease in advected moisture flux from the prevailing winds, see Figure 013.

5.5 Uncertainty in Model Estimates

Model uncertainty exists in many sources, including the initial condition, the boundary conditions, within the scale limitations of the resolved processes, the mechanics of the model processes and the parameters that govern the processes. In limited area models, there is also variability in the lateral boundary conditions. For the current research, this variability can affect the differences detected between the two scenarios, potentially impacting results. Ideally, this variability space can be explored in depth, perhaps using ensembles over multiple decades, including differing starting years and perturbations. The range of the variability space that can be sampled is limited by computational expense of the simulations. The four year simulations presented here took approximately two months each using 96 parallel computational cores with high-speed interconnects, the significant computational time being an result of the highly memory intensive ecosystem model and atmospheric time-stepping that is relatively short (30 seconds) compared to general circulation models. However, we maintain that the the pattern differences in precipitation and evaporation between the two scenarios were consistent to merit commentary.

Recall that the *Actual* scenario's simulations were compared to a group of different observations with the intention of verifying the modeling system's ability to represent key processes. The model's regional demographic of vegetation biomass was compared to field inventory data, atmospheric thermodynamic profiles were compared to soundings, mean all-sky profiles of cloud water were compared to satellite estimates and the seasonality of precipitation, net-radiation, latent heat flux and sensible heat flux were compared with multi-data composite data products (see Appendices A2,A3,A4,A5 and A6). The comparisons with observations (which harbour their own uncertainty) suggest the model system is adequate to make a meaningful comparison between the two scenarios, yet not without room for improvement.

A small selection of published research has conducted similar simulations to those reported here, with results that offer limited comparison. Perhaps most similar, Bagley et al. compared differential land-cover scenarios similar to our *Potential* and *Actual* vegetation, finding a generally weaker differential patterning of precipitation. However, evidence of the strongest pattern differnces also occured south of the Amazon delta, which may be viewed as correlated with the depression in the precipitation dipole presented in this work. The simulations conducted by Bagley et al. also used a different modeling system (The Weather Research and Forecasting System WRF) and land-surface model (Noah LSM), suggesting that model intercomparison would be a useful endeavor in rectifying the regional hydrometeorological effects of South American land-cover change. Even the choice of module parameterization alone can be a significant source of variability.

Other studies have used similar simulation approaches, but targetted land-atmosphere effects under future conditions. Global simulations conducted by Medvigy et al. found that future business as usual (aggressive) deforestation would generate dipole precipitation differential with respect to conservative deforestation scenarios. The length scales of the patterning in the dipoles (100s of kilometers) showed similarity with results presented here. However, the differential pattern locations were significantly different, as were the differntial land-use scenarios. Walker et al. also evaluated the effects of future deforestation scenarios on the regional hydrometeorology, finding that massive deforestation outside of protected areas will lead to significant basin-wide changes in rainfall, both positive and negative. In summary, there are some commonalities between the various regional simulations, albeit from differing land-use scenarios; impacts on hydrometeorological climate are expressed most strongly as changes in dry-season precipitation, and that patterning exists to varying degrees at large length scales (> 100 kilometers) (Walker et al., 2009), (Bagley et al., 2014) and (Medvigy et al., 2011).

6 Conclusions

The simulation results support that historical land conversion has influenced the patterning of South American precipitation. Two distinct differential precipitation patterns emerged in the simulations, where mean annual precipitation showed moderate yet consistent differences. One dipole occured near Eastern Pará Brazil, and another pattern occured near the Gran Chaco region of the Peru-Bolivia border. An assessment of regional moisture stress indices indicate that terrestrial vegetation in these two regions have moderate (Pará) and significant (Gran Chaco) susceptibility to changes in water availability.

The simulations suggest land conversion in South America has not had a significant influence on continental mean

precipitation. Continental mean precipitation with land conversion decreased in three out of four simulation years, but the differences were insignificant. On the other hand, differences in mean continental runoff (increased with human land-conversion) and total evapotranspiration (decreased with human land-conversion) were consistent and significant from year to year.

The differences in precipitation at Pará Brazil are more strongly connected with localized differences in land-surface energy fluxes. The hydrometeorological analysis near Gran Chaco suggests that human land-conversion has to some extent impacted the strength of the South American moisture circulation in the South Western portion of the Amazon, which claims partial responsibility along with differential surface fluxes for an estimated decrease in annual precipitation in the Gran Chaco.

A1 Land-Atmosphere Model Coupling

The atmospheric model (BRAMS) and the land surface model (ED2) are loosely and asynchronously coupled. This assumes that the two models pass each other boundary conditions at a frequency that captures the natural variability of the flux, yet the fluxes between models are not dynamically changing as prognostic variables within the numerical integrator sub-stepping. The atmosphere (BRAMS) provides information at the beginning of the ED2 forward step, while ED2 assumes this information is constant over the duration of its forward step and makes a time average of the fluxes during the step to return.

Meso-scale atmospheric models at spatial resolutions of tens of kilometers typically perform integrations on the order of tens of seconds to maintain numerical stability and convergence. The simulations in this work used an atmospheric time-step of 30 seconds (for non-accoustic dynamics, accoustics were 10 seconds). Ideally, the land surface and atmospheric models operate at time-steps that approach the infintessimaly small. The ED2 has a non-trivial computational overhead due to the large number of vegetation cohorts experiencing energy balancing within each grid cell. Ultimately, the ED2.1 model used a 120 second time-step while coupled to BRAMS.

Atmospheric variables such as air temperature, humidity and wind-speed are provided to ED2 at a reference height of 70 meters. This is required because ED2 internally calculates turbulent transport of heat, moisture and momentum through the canopy and into the inertial sub-layer of the lower atmosphere. The turbulent transport of scalars through the sub-layer above the canopy were calculated following Beljaars and Holtslag. These calculations relied on gradients that were baseed on the enthalpy, density and specific humidity of air at reference temperature and within the canopy interstitial airspace. A list of the variables required to drive ED2 is provided in Table 05.

The ED2 model passes boundary fluxes at the grid scale to the atmospheric surface layer as an area-weighted average across patches. There are three groups of information the land surface must provide the atmosphere model: 1) the topography which governs the geometry of the atmosphere's coordinate system and drag, 2) a lower boundary condition for turbulent closure, i.e., the vertical velocity perturbations of momentum, heat, moisture and carbon, and 3) a surface albedo for the atmospheric radiative transfer calculations. These variables are listed in Table 06. Because the ED2 model prognoses spatial variables at the patch sale (such as canopy temperature, humidity, etc), spatial averaging is required for flux variables. For any generic variable S, at a grid cell with M patches of area A_{patch}, the area averaged quantity is straight forward.

$$S_{grid} = \sum_{j}^{M} S_{patch,j} A_{patch,j} \tag{A1}$$

$$\sum_{j}^{M} A_{patch,j} = 1 \tag{A2}$$

More detailed explanation of how turbulent fluxes are calculated in the ED2 model can be found in Medvigy et al. (2009) and Knox (2012).

A2 Regional Above Ground Biomass

The model estimated equilibrium live above ground biomass (AGB) and basal area (BA) that represent the initial condition is compared with a collection of census measurements in (Baker et al., 2004a)(Baker et al., 2004b), see Figure 017. A map is provided showing the locations of the plot experiments, see Figure 018. The coordinates from the measurement stations were matched with ED2 nearest neighbor grid cells. Consistent with observations, only ED2 plants greater than 10cm in primary forests were included in the comparison. The published measurements were taken at different times over the previous decades, the lag between these sites and the time of the simulation initial condition (January 2008) varies and is reported. Tree diameters in ED2 is diagnosed allometrically from structural carbon, similar to allometric equations in (Chave et al., 2001) and (Baker et al., 2004b), with differences in parametrization to reflect functional groups.

The majority of sites show fair agreement with model estimated above ground biomass and basal area. The exception to this is the cluster of sites located in eastern Bolivia at Huanchaca Dos (HCC), Chore 1 (CHO), Los Fierros Bosque (LFB) and Cerro Pelao (CRP). There are several potential reasons for this discrepancy attributed to the model such as: variability in 1) climate forcing data (most notably precipitation and vapor pressure deficit as these are water limited growth conditions), 2) edaphic conditions and 3) plant

functional parameters. These plots are close to the southern Amazonian transition between tropical rain-forests and Cerrado type open canopy forests where gradients in vegetation types are large and uncertainty is expected to be greater. Large spatial gradients in biomass are also reflected in the differences among the cluster of plots (HCC, CHO, LFB and CRP), ($124.8\ \mathrm{Mg\,ha^{-1}}$ above ground biomass at CHO and $260.0\ \mathrm{Mg\,ha^{-1}}$ AGB at HCC). The sharp gradient in forest biomass suggests that the omission of sub-pixel variability in the modified DS314 climate forcing could explain a portion of this difference, along with any persistent biases.

A3 Thermodynamic Mean Profiles

The objectives of this experiment require that modeling system output match mean observations to such a degree that there is trust in the model's ability to represent physical processes. It is believed that the relative differences between the two simulations have validity if model processes reproduce mean observed tendencies in the land surface and atmosphere.

Mean monthly profiles of model estimated air temperature, specific humidity and moist static energy are compared with mean radiosonde data over Manaus Brazil (see Figures 019 and 020). Comparisons are made at 00:00Z UTC (8pm local time) and 12:00Z UTC (8am local time). The model estimates a consistently warmer atmosphere, in the range of about two degrees both morning and evening. Model estimated specific humidity in the lower troposphere is lower than the radiosondes, see Figure 019. Moist static energy is slightly underestimated by the model in the lower troposphere and then overestimated in the mid to upper troposphere. This may suggest that the model is convecting relatively large quantities of warm moist air at the surface and entraining it to the upper atmosphere.

A4 Inter-seasonal Precipitation and Surface Radiation

Monthly precipitation and down-welling shortwave radiation in the model is evaluated as spatial means within five separate zones of analysis. The boundaries of the zones of analysis are shown in Figure 018. Monthly mean model estimates are again compared to precipitation estimates from the Tropical Rainfall Measurement Mission (TRMM) 3B43 product and surface radiation from the Global Energy and Water Exchanges Project (GEWEX) Surface Radiation Budget (SRB) product. There is generally acceptable agreement between the model and TRMM estimated precipitation. The seasonal variability in both datasets is greater than their differences, see Figure 021. The most significant differences are the strength of of the wet-season peak precipitation in Zone 3 (central-eastern Amazon) and the severity of the dry season precipitation in Zone 5 (Southern Brazil). The timing of peak and minimum rainfall show generally good agreement, particularly in Zones 2-5. The lower estimate of mean precipitation in Southern Brazil is consistent with decreased cloud albedo and increased down-welling short-wave radiation at the surface, see Figure 022. Surface shortwave radiation has a modest under-estimating bias compared with the SRB estimates for most other cases.

A5 Inter-seasonal Latent and Sensible Heat Flux

Similar to the comparison in Appendix A4, monthly mean model estimated latent (see Figure 023) and sensible heat flux (see Figure 024) are compared with means from a benchmark. In this case, we compare output with the products of (Jung et al., 2011). The Jung et al. products are based off of surface observations, which are upscaled using gridded explanatory variables from various sources including the Climate Research Unit (CRU), Global Precipitation Climatology Centre (GPCC) as well as the ERA-Interim product used in this study. The inter-seasonal means also incorporate spatial means within the domains shown in Figure 018.

The purpose of this comparison is to give some benchmark of the ecosystem model's ability to partition energy flux at the land-surface. The patterned flux of energy is dependant on the atmospheric model and its lateral boundary conditions as well. Precipitation, cloud cover and atmospheric radiation scattering will have strong effects on available surface water to be converted into latent heat, as well as the energy incident on the land-surface which drives total energy exchange. This is particularly true when looking at seasonal means, total energy flux is strongly controlled by energy entering the land-surface.

Compared to the synthesis product, the model system estimated a stronger inter-seasonal variability of latent and sensible heat flux over Southern Brazil and the South American Convergence zone. Both model and observations showed relatively less seasonal variability over the Amazon. In these regions, the model estimated a positive bias in latent heat flux and very little bias in sensible heat flux.

A6 All-Sky Cloud Water Content Profiles

Cloud profile validation datasets were constructed from CloudSat Cloud Water content (2B-CWC-RO) and Cloud Classification (2B-CLDCLASS-LIDAR) datasets. [3] Overpasses during February 2007-2011 that intersected the geographic subset between 3^oN-12^oS and 70^oW-55^oW were collected and interpolated to a constant vertical datum above the surface. Overpasses typically occurred near 17hrs UTC.

Making a rigorous comparison of the model estimated cloud water and observation is a significant challenge. Consider that the simulation time frame does not overlap with the CloudSat mission time-frame, so these comparisons are treated as proxies to climatology and not weather validation.

[3] Cloudsat data sets were provided on-line by CloudSat Data Processing Center, courtesy of NASA, Colorado State University and their partners.

CloudSat measurements are known to have signal loss, attenuation and clutter during moderate to intense rainfall; events such as these could not be filtered from the comparison. It must also be assumed that the cloud classification algorithm is not without error. Nonetheless, the purpose of the comparison was to get a sense of whether the simulations estimated reasonable mean ranges of water contents and cloud fractions, and also if the phase transitions (liquid to ice) were occurring at reasonable elevations.

The all-sky cloud water content profiles for both cumulus and non-cumulus clouds are provided in Figure 025. The peaks in model estimated mean cloud water content showed reasonable agreement across liquid and ice cloud types. The model estimated generally more water content in both phases, skewed towards higher altitudes and showed a uni-modal shape in the vertical distreribution. It is possible that CloudSat relative underestimation could be explained by the omission of precipitating clouds.

Acknowledgements. This work was made possible through both the National Science Foundation Grant ATM-0449793 and National Aeronautics and Space Administration Grant NNG06GD63G. The authors would like to thank D. Entekhabi and E.A.B Eltahir for their generous discussion and council. Further, the anonymous peer reviewers provided us with thorough, challenging and fair recommendations. We believe their efforts have contributed to significant improvements to this manuscript and we thank them.

References

Albani, M., Medvigy, D., Hurtt, G. C., and Moorcroft, P. R.: The contributions of land-use change, CO2 fertilization, and climate variability to the Eastern US carbon sink, Global Change Biology, 12, 2370–2390, 2006.

Anthes, R. A.: Enhancement of convective precipitation by mesoscale variations in vegetative covering in semiarid regions, J. of Climate and Applied Meteorology, 23(4), 541–554, 1984.

Bagley, J., Desai, A., Harding, K., Synder, P., and Foley, J.: Drought and deforestation: Has land cover change influenced recent precipitation extremes in the Amazon?, Journal of Climate, 27, 345–361, 2014.

Baker, T., Phillips, O., Malhi, Y., Almeida, S., Arroyo, L., Fiore, A. D., Erwin, T., amd T.J. Killeen, N. H., Laurance, S., Laurance, W., Lewis, S., Monteagudo, A., Neill, D., Vargas, P., Pitman, N., Silva, N., and Vasquez-Martinez, R.: Increasing biomass in Amazonian forest plots, Phil. Trans. R. Soc. Lond. B, 359, 353–365, 2004a.

Baker, T., Phillips, O., Malhi, Y., Almeida, S., Arroyo, L., Fiore, A. D., Erwin, T., Killeen, S., Laurance, S., Laurance, W., Lewis, S., Lloyd, J., Monteagudo, A., Neill, D., Patino, S., Pitman, N., Silva, N., and Martinez, R. V.: Variation in wood density determines spatial patterns in Amazonian forest biomass, Global Change Biology, 10, 545–562, 2004b.

Baldi, M., Dalu, G. A., and Pielke, R. A.: Vertical velocities and available potential energy generated by landscape variability - theory., J. of Applied Meteorology and Climatology, 47(2), 397–410, 2008.

Beljaars, A. C. M. and Holtslag, A. A. M.: Flux Parameterization over Land Surfaces for Atmospheric Models, J. Appl. Meteor., 30, 327–341, 1991.

Cardille, J. and Foley, J.: Agricultural Land-use Change in Brazilian Amazonia Between 1980 and 1995: Evidence from Integrated Satellite and Census Data, Remote Sensing of Environment, 87, 551–562, 2003.

Chambers, J., Higuchi, N., and Schimel, J.: Ancient trees in Amazonia, NATURE, 391, 135–136, 1998.

Chave, J., Riera, B., and Dubois, M.: Estimation of biomass in a neotropical forest of French Guiana: spatial and temporal variability, Journal of Tropical Ecology, 17, 79–96, 2001.

Chave, J., Muller-Landau, H. C., Baker, T. R., Easdale, T. A., Ter Steege, H., and Webb, C. O.: Regional and phylogenetic variation of wood density across 2456 neotropical tree species, ECOLOGICAL APPLICATIONS, 16, 2356–2367, 2006.

Chen, C. and Cotton, W.: A One-Dimensional Simulations of the Stratocumulus-Capped Mixed Layer, Boundary Layer Meteorology, 25(3), 289–321, 1983.

Collatz, G., Ribas-Carbo, M., and Berry, J.: Coupled Photosynthesis-Stomatal Conductance Model for Leaves of C_4 Plants, Aust. J. Plant Physiol., 19, 519–538, 1992.

Collatz, G. J., Ball, J., Grivet, C., and Berry, J. A.: Physiological and environmental regulation of stomatal conductance, photosynthesis and transpiration: a model that includes a laminar boundary layer, Agric. For. Meteorol., 54, 107 – 136, 1991.

Cotton, W., Pielke, R., Walko, R., Liston, G., Tremback, C., Jiang, H., McAnelly, R., Harrington, J., Nicholls, M., Carrio, G., and McFadden, J.: RAMS 2001: Current status and future directions, Meteorol Atmos Phys, 82, 5–29, 2003.

d'Almeida, C., Vörösmarty, C. J., Hurtt, G. C., Marengo, J. A., Dingman, S. L., and Keim, B. D.: The effects of deforestation on the hydrological cycle in Amazonia: a review on scale and resolution, Intl. J. Climatol., 27, 633–647, 2007.

Dalu, G. A., Pielke, R. A., Baldi, M., and Zeng, X.: Heat and momentum fluxes induced by thermal inhomogeneities, J. of Atm. Sci, 53(22), 3286–3302, 1996.

Dee, D. and co authors: The ERA-Interim reanlysis: configuration and performance of the data assimilation system, Quarterly Journal of the Royal Meteorological Society, 137(656), 553–597, 2011.

Dickinson, R. and Henderson-Sellers, A.: Modeling Tropical Deforestation: A Study of GCM Land-Surface Parameterization, Q. J. Royal Meteorological Soc., 114, 1998.

Dietze, M., Wolosin, M., and Clark, J.: Capturing diversity and interspecific variability in allometries: A hierarchical approach, Forest Ecology and Management, 256, 1939–1948, 2008.

Eltahir, E.: Role of Vegetation in Sustaining Large-Scale Atmospheric Circulations in the Tropics, J.G.R. Atmospheres, 10(D2), 1996.

Eltahir, E. and Bras, R.: On the Response of the Tropical Atmosphere to Large-Scale Deforestation, Q.J.R. Meteorol. Soc., 119, 779–793, 1993.

Eltahir, E. A. B. and Bras, R.: Precipitation recyling in the Amazon basin, Q. J. Royal Meteorological Soc., 120, 861–880, 1994.

Freitas, S. R., Rodrigues, L. F., Longo, K. M., and Panetta, J.: Impact of a monotonic advection scheme with low numerical diffusion on transport modeling of emissions from biomass burning, J. Adv. Model. Earth Syst., 4, n/a–n/a, 2012.

Geist, H. and Lambin, E.: Proximate Causes of Underlying Driving Forces of Tropical Deforestation, Bioscience, 52(2), 2002.

Grell, G. A. and Dévényi, D.: A generalized approach to parameterizing convection combining ensemble and data assimilation techniques, Geophys. Res. Lett., 29, 38–1–38–4, 2002.

Harrington, J. and Olsson, P.: A Method for the Parameterization of Cloud Optical Properties in Bulk and Bin Microphysical Models. Implications for Arctic Cloud Boundary Layers, Atmospheric Research, 57, 51–80, 2001.

Henderson-Sellers, A., Dickinson, R., Durbridge, T., Kennedy, P., McGufie, K., and Pitman, A.: Tropical Deforestation: Modeling Local to Regional Scale Climate Change, Journal Geophysical Research, 98, 7289–7315, 1993.

Hurtt, G., Frolking, S., Fearon, M., III, B. M., Shevialokova, E., Malyshew, S., Pacala, S., and Houghton, R.: The underpinnings of land-use history: three centuries of global gridded land-use transitions, wood harvest activity and resulting secondary lands., Global Change Biology, 12, 1–22, 2006.

INPE: Monitoring of the Amazon forest by satellite 2001-2002, Instituto Nacional de Pesquisas Espaciais, Technical Paper, Sao Jose Dos Campos, Brazil, 2003.

Jung, M., Reichstein, M., and Bondeau, A.: Towards global empirical upscaling of FLUXNET eddy covariance observations: validation of a model tree ensemble approach using a biosphere model, Biogeosciences, 6, 2001–2013, 2009.

Jung, M., Reighstein, M., Margolis, H., Cescatti, A., Richardson, A., Arain, M. A., Arneth, A., Bernhofer, C., Bonal, D., Chen, J., Gianelle, D., Gobron, N., Kiely, G., Kutsch, W., Lasslop, G., Law, B., Lindroth, A., Merbold, L., Montagnani, L., Moors, E. J., Papale, D., Sottoconrola, M., Vaccari, F., and Williams, C.: Global Patterns of Land-Atmosphere Fluxes of Carbon Dioxide, Latent Heat, and Sensible Heat Derived from Eddy Covariance, Satellite and Meteorological Observations, Journal of Geophysical Research, 116(G3), 1–16, 2011.

Kain, J.: The Kain-Fritsch Convective Parameterization: An Update, Journal of Applied Meteorology, 43(1), 170–181, 2004.

Kain, J. and Fritsch, J.: A One-Dimensional Entraining-Detraining Plume Model and Its Application in Convective Parameterization, Journal of Atmospheric Science, 47(23), 2784–2802, 1990.

Kleidon, A. and Heimann, M.: Assessing the Role of Deep Rooted Vegetation in the Climate System with Model Simulations: Mechanism, Comparison to Observations and Implications for Amazonian Deforestation, Climate Dynamics, 16, 183–199, 2000.

Knox, R.: Land Conversion in Amazonia and Northern South America; Influences on Regional Hydrology and Ecosystem Response, Ph.D. thesis, Massachusetts Institute of Technology, Cambridge, Massachusetts, USA, 2012.

Knox, R., Bisht, G., Wang, J., and Bras, R.: Precipitation Variability over the Forest-to-Nonforest Transition in Southwestern Amazonia, Journal of Climate, 24, 2368–2377, 2011.

Lammering, B. and Dwyer, I.: Improvement of Water Balance in Land Surface Schemes by Random Cascade Disaggregation of Rainfall, International Journal of Climatology, 20, 681–695, 2000.

Laurance, W., Cochrane, M., Bergen, S., Fearnside, P., Delamonica, P., Barber, C., D'Angelo, S., and Fernandes, T.: The future of the Brazilian Amazon, Science, 291(5503), 2001.

Laurance, W., Nascimento, H., Laurance, S., Condit, R., D'Angelo, S., and Andrade, A.: Inferred longevity of Amazonian rainforest trees based on a long-term demographic study, FOREST ECOLOGY AND MANAGEMENT, 190, 131–143, 2004.

Lean, J. and Warrilow, D.: Simulation of the Regional Climatic Impact of Amazon Deforestation, Nature, 342, 411–413, 1989.

Leuning, R.: A critical appraisal of a combined stomatal-photosynthesis model for C3 plants, Plant Cell Environ., 18, 339–355, 1995.

Massman, W.: An Analytical One-Dimensional Model of Momentum Transfer by Vegetation of Arbitrary Structure, Boundary Layer Meteorology, 83, 407–421, 1997.

Medvigy, D., Wofsy, S., Munger, J., Hollinger, D., and Moorcroft, P.: Mechanistic scaling of ecosystem function and dynamics in space and time: Ecosystem Demography model version 2, Journal of Geophysical Research, 114(G01002), 1–21, 2009.

Medvigy, D., Walko, R., Otte, M., and Avissar, R.: The Ocean-Land-Atmosphere-Model: Optimization and Evaluation of Simulated Radiative Fluxes and Precipitation, Monthly Weather Review, 138(5), 1923–1939, 2010.

Medvigy, D., Walko, R., and Avissar, R.: Effects of Deforestation on Spatiotemporal Distributions of Precipitation in South America, Journal of Climate, 24, 2147–2163, 2011.

Moorcroft, P., Hurtt, G., and Pacala, S.: A Method for Scaling Vegetation Dynamics: The Ecosystem Demography Model, Ecological Monographs, 71(4), 557–586, 2001.

Munoz-Villers, L. E. and McDonnell, J. J.: Land use change effects on runoff generation in a humid tropical montane cloud forest region, HYDROLOGY AND EARTH SYSTEM SCIENCES, 17, 3543–3560, 2013.

Nakanishi, M. and Niino, H.: An improved Mellor-Yamada level-3 model with condensation physics: its numerical stability and application to a regional prediction of advection fog., Boundary-Layer Meteor, 119, 397–407, 2006.

Nepstad, D., de Carvalho, C., Davidson, E., Jipp, P., Lefebvre, P., Negreiros, H., dal Silva, E., Stone, T., Trubore, S., and Vieira, S.: The Role of Deep Roots in the Hydrological and Carbon Cycles of Amazonian Forests and Pastures, Nature, 372, 666–669, 1994.

Nepstad, D., Carvalho, G., Barros, A., Alencar, A., Capobianco, J., amd P. Moutinho, J. B., Lefebvre, P., Silva, U. L., and Prins, E.: Road paving, Fire Regime Feedbacks and the Future of Amazon Forests, Forest Ecology and Management, 154, 395–407, 2001.

Nobre, C., Sellers, P., and Shukla, J.: Amazonian Deforestation and Regional Climate Change, Journal of Climate, 4, 1991.

Peilke, R.: Land Use and Climate Change, Science, 310, 1625–1626, 2005.

Pielke, R.: Influence of the spatial distribution of vegetation and soils on the prediction of cumulus convective rainfall., Reviews in Geophysics, 39(2), 151–171, 2001.

Poorter, L., Bongers, L., and Bongers, F.: Architecture of 54 moist-forest tree species: traits, trade-offs and functional groups, Ecology, 87(5), 1289–1301, 2006.

Quesada, C., Lloyd, J., Anderson, L., Fyllas, N., Schwarz, M., and Czimczik, C.: Soils of Amazonia with particular reference tot he RAINFOR sites, Biogeosciences, 8, 1415–1440, 2011.

Rossato, L.: Estimativa da capacidade de armazenamento de água no solo do Brasil, Msc. thesis, Instituto Nacional de Pesquisas Espaciais (INPE), São José dos Campos, Brazil, in Portuguese, 2001.

Scholes, R., Skole, D., and (eds.), J. I.: A Global Database of Soil Properties: Proposal for Implementation. Report of the Global Soils Task Group, Tech. Rep. IGBP-DIS Working Paper 10a, International Geosphere-Biosphere Programme - Data and Information System (IGBP-DIS). University of Paris, Paris, France, 1995.

Sheffield, J., Goteti, G., and Wood, E.: Development of a 50-Year High-Resolution Global Dataset of Meteorological Forcings for Land Surface Modeling, Journal of Climate, 19, 3088–3111, 2006.

Silva, R. R. D., Werth, D., and Avissar, R.: Regional impacts of future land-cover changes on the Amazon basin wet-season climate, Journal of Climate, 21(6), 1153–1170, 2008.

Skole, D. and Tucker, C.: Tropical Deforestation and Habitat Fragmentation in the Amazon: Satellite Data from 1978 to 1988, Science, 260(5116), 1905–1910, 1993.

Soares-Filho, B. S. and co authors: Modelling conservation in the Amazon basin, Nature, 440(23), 520–523, 2006.

Tremback, C. and Kessler, R.: A surface temperature and moisture parameterization for use in mesoscale models, Preprints, Seventh Conf. on Numerical Weather Prediction, Montreal, PQ, Canada, Amer. Meteor. Soc., p. 355–358, 1985.

Walcek, C. and Aleksic, N.: A simple but accurate mass conservative, peak-preserving, mixing ratio bounded advection algorithm with Fortran code., Atmos. Environ., 32, 3863–3880, 1998.

Walker, R., Moore, N., Arima, E., Perz, S., Simmons, C., Caldas, M., Vergara, D., and Bohrer, C.: Protecting the Amazon with protected areas, Proceedings of the National Academy of Sciences of the United States of America, 106(26), 10 582–10 586, 2009.

Walko, R., Band, L., Baron, J., Kittel, T., Lammers, R., Lee, T., Ojima, D., Pielke, R., Taylor, C., Tague, C., Tremback, C., and Vidale, P.: Coupled atmosphere-biophysics-hydrology models for environmental modeling, Journal of Applied Meteorology, 39, 931–944, 2000.

Wang, J., Chagnon, F., Williams, E., Betts, A., Renno, N., Machado, L., Bisht, G., Knox, R., and Bras, R.: The impact of deforestation in the Amazon basin on cloud climatology, Proceedings of the National Academy of Science, 106(10), 3670 –3674, 2009.

Zhao, W. and Qualls, R. J.: A multiple-layer canopy scattering model to simulate shortwave radiation distribution within a homogeneous plant canopy, Water Resour. Res., 41, W08 409, 2005.

Zhao, W. and Qualls, R. J.: Modeling of long-wave and net radiation energy distribution within a homogeneous plant canopy via multiple scattering processes, Water Resour. Res., 42, W08 436, 2006.

Zimmermann, B., Elsenbeer, H., and De Moraes, J.: The influence of land-use changes on soil hydraulic properties: Implications for runoff generation, FOREST ECOLOGY AND MANAGEMENT, 222, 29–38, 2006.

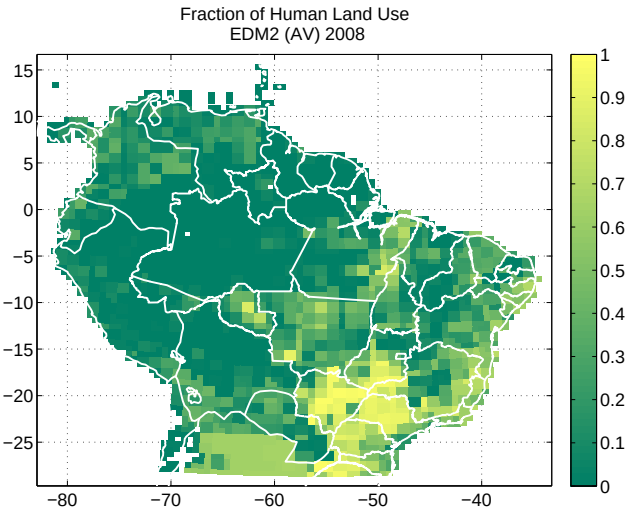

Fig. 01. Fraction of the land surface with human land-use. Output is taken from the ED2 the *Actual Vegetation* (AV) simulation, which was driven with Global Land Use (GLU) and SIMAMAZONIA-1 land-use transition data.

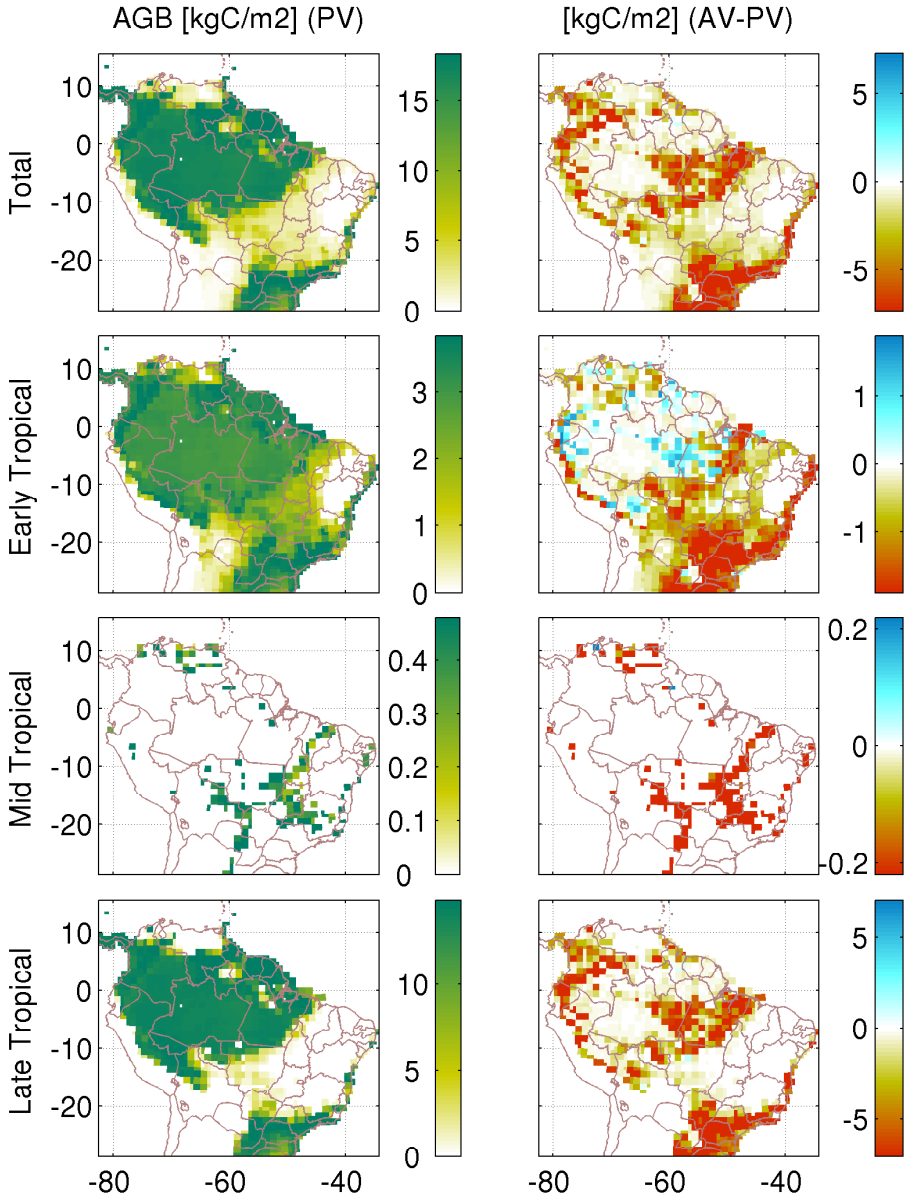

Fig. 02. Regional maps of total above ground biomass (AGB) [$\mathrm{kg\,m^{-2}}$] from the ED2 initial condition. The left column indicates results are from the *Potential* Vegetation condition, the right column is the relative differences between the *Actual* and *Potential* scenarios, $(AGB_{AV} - AGB_{PV})$. Each row represents the partitioning of the above ground biomass into respect plant functional types. "Early Tropical", "Mid Tropical" and "Late Tropical" refer to broad-leaf tropical evergreen plant functional types.

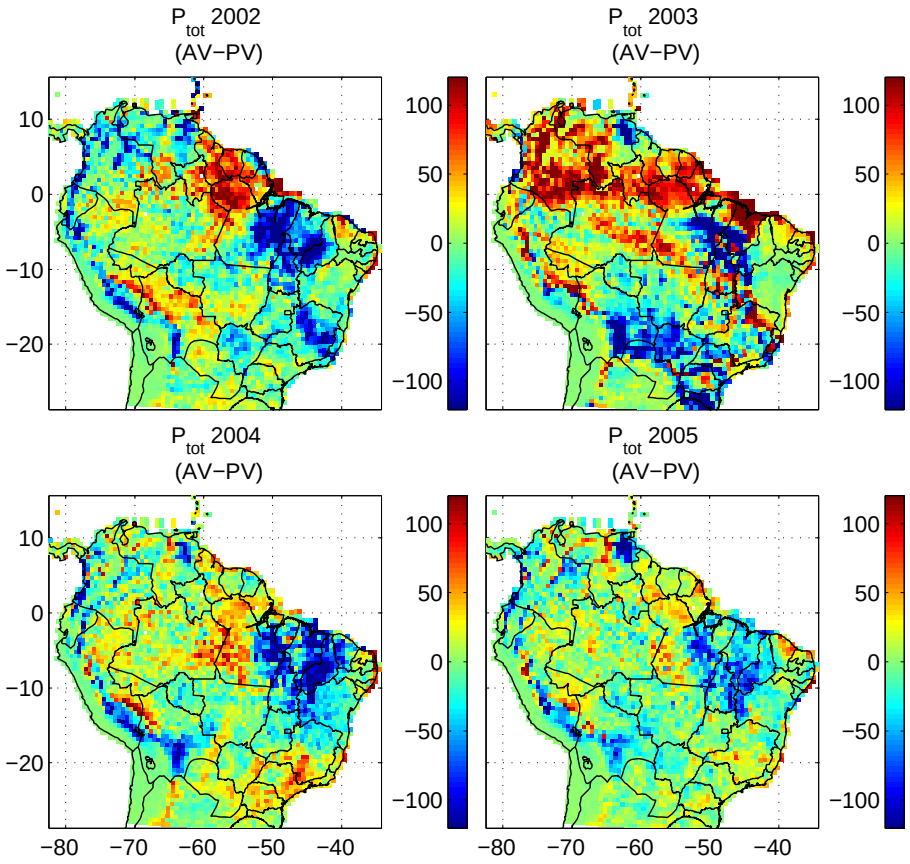

Fig. 03. Differences in total annual surface precipitation [mm], 2002-2005. The *Potential* Vegetation (PV) Condition is subtracted from the *Actual* Vegetation (AV) condition, (AV-PV).

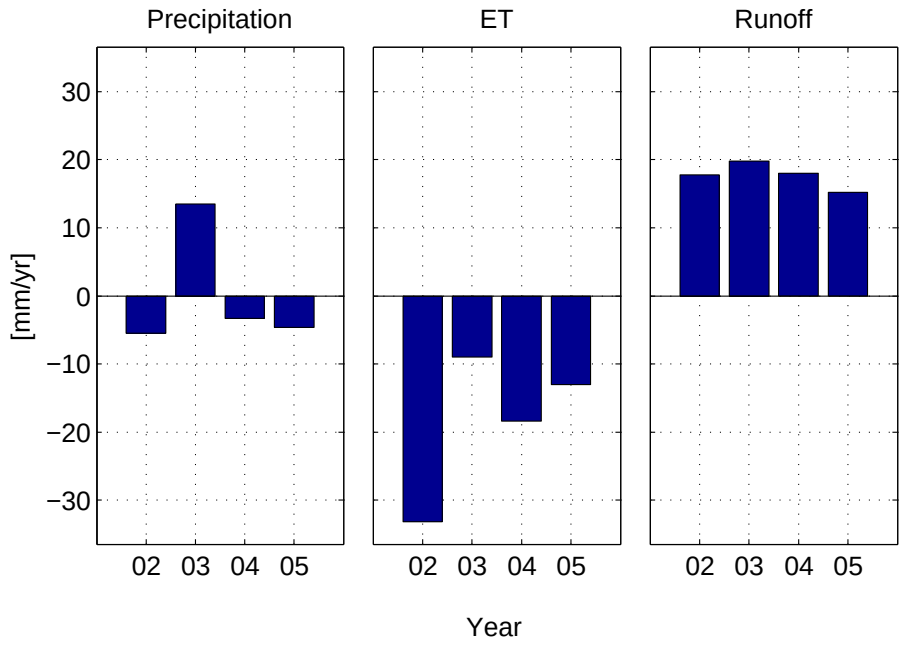

Fig. 04. Difference in mean continental precipitation, evaporation and total runoff, between the *Actual* Vegetation case and *Potential* Vegetation case (AV-PV).

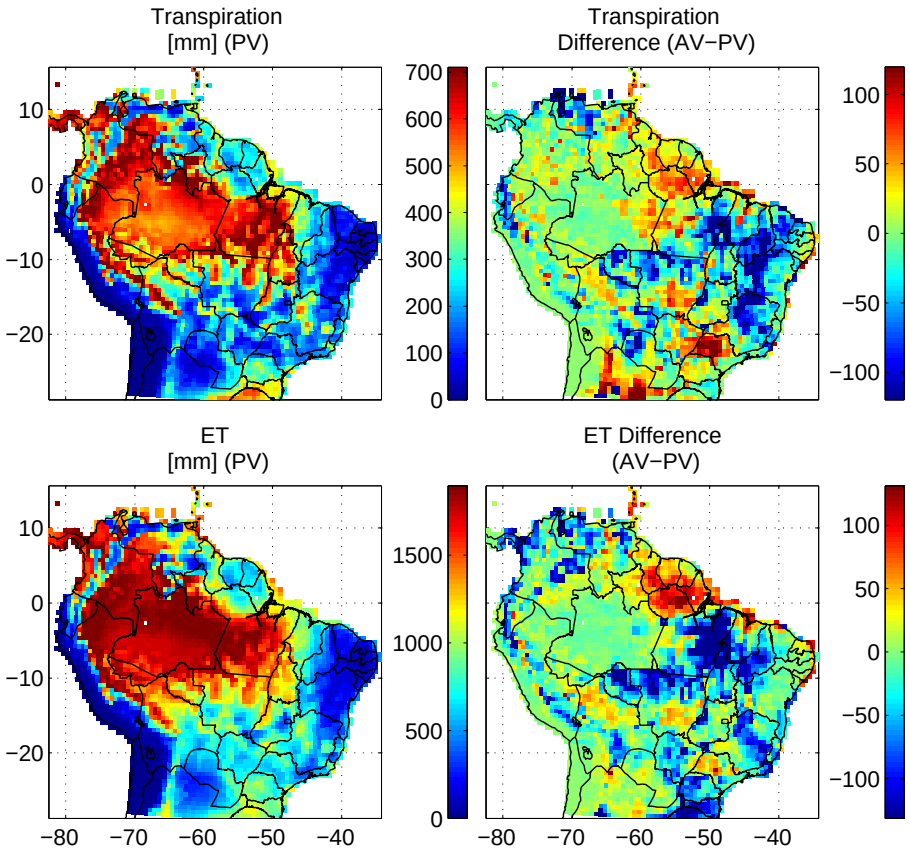

Fig. 05. Left Panels: Mean annual transpiration and evapotranspiration in the *Potential* vegetation (PV) scenario, from 2002-2005 [mm]. Right panels: difference in mean annual transpiration and evapotranspiration between the *Actual* Vegetation case and *Potential* Vegetation case (AV-PV).

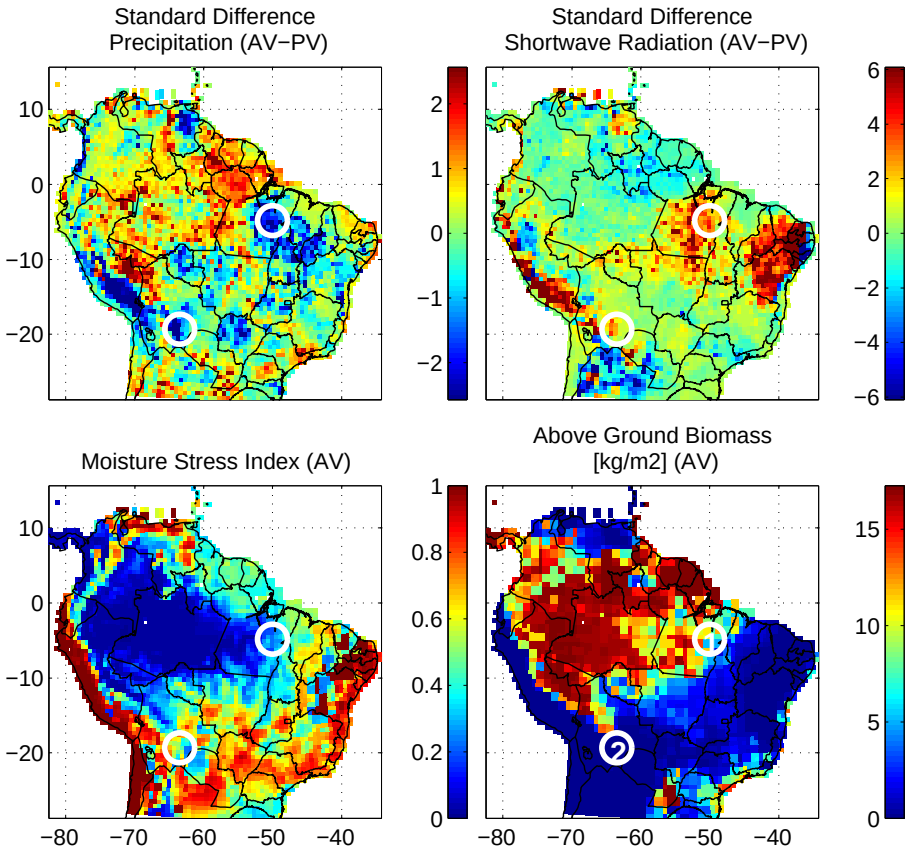

Fig. 06. Combined assessment of the regional significance in differences between precipitation and radiation, and the susceptibility of the ecosystems. Upper panels show standard scores for consistency of differences *Actual* and *Potential* (AV-PV) surface precipitation and surface down-welling shortwave radiation. The lower left panel shows the moisture stress index for the *Actual* (AV) scenario, see Equation (3). For reference, *Actual* (AV) scenario Above Ground Biomass is provide in the bottom right panel.

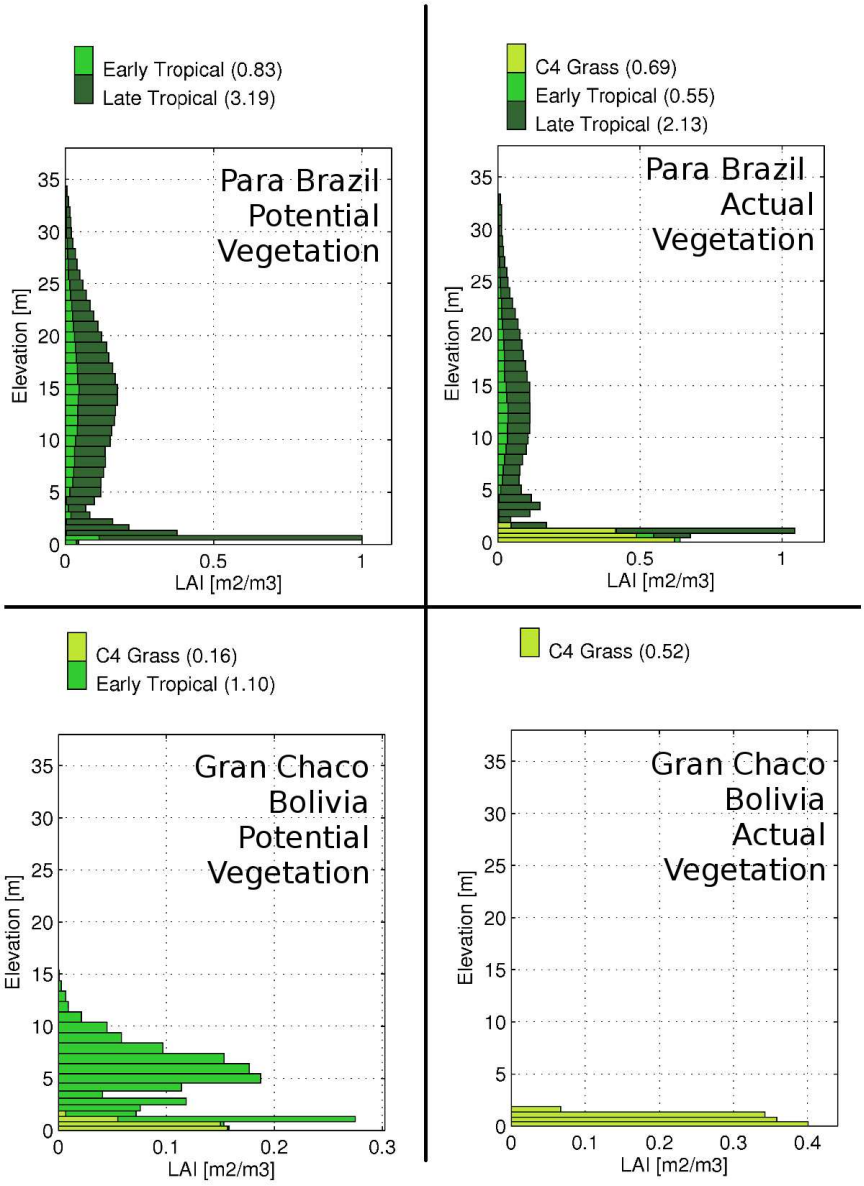

Fig. 07. Mean vertical leaf area index profiles $[m^2 m^{-3}]$ estimated by the Ecosystem Demography Model 2 at the two focus areas. Vertically integrated leaf area index $[m^2 m^{-2}]$ per each represented functional type of plant is shown in the key above each plot.

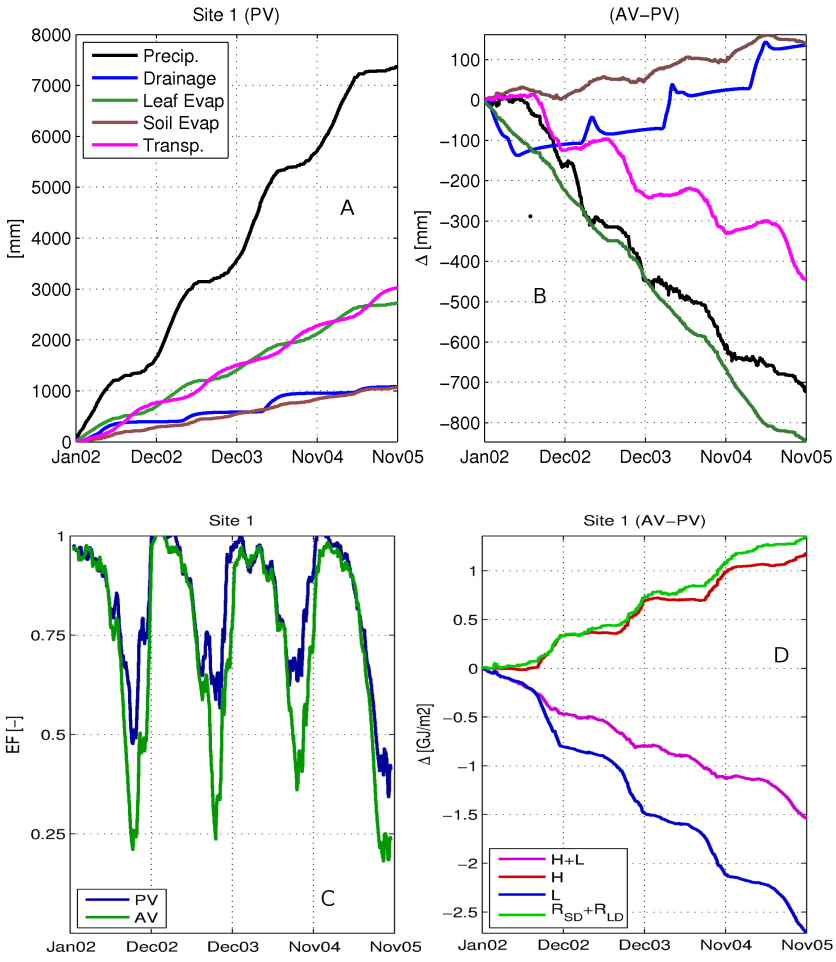

Fig. 08. Time series analysis of the surface water and energy balance at the Pará focus site, 2002-2005. Upper left panel (A): Accumulated water flux for the *Potential* scenario. Upper right panel (B): Accumulated differential water flux between *Actual* (AV) and *Potential* (PV) scenarios. Lower left panel (C): mean evaporative fraction, latent heat flux (L) divided by the sum of latent and sensible (H) heat flux (L/(H+H)). Lower right panel (D): accumulated differential energy flux in GigaJoules per square meter. R_{SD} is down-welling short-wave radiation incident on the surface, R_{LD} is down-welling long-wave radiation incident on the surface.

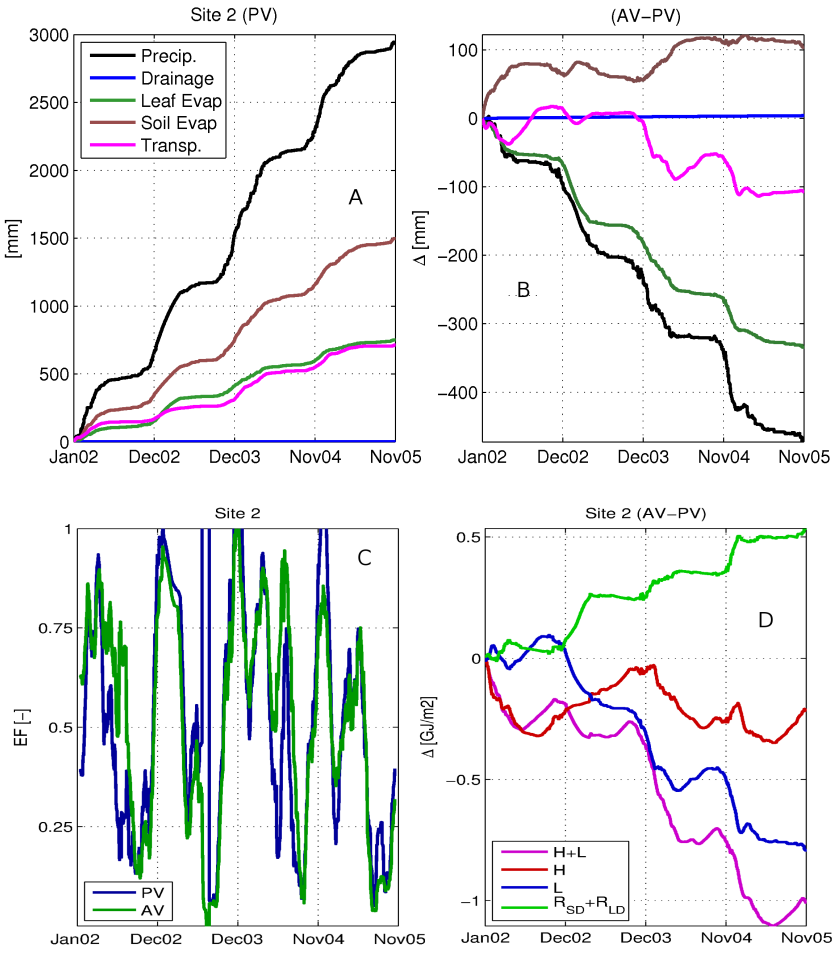

Fig. 09. Time series analysis of the surface water and energy balance at the Gran Chaco site, 2002-2005. Upper left panel (A): Accumulated water flux for the *Potential* scenario. Upper right panel (B): Accumulated differential water flux between *Actual* (AV) and *Potential* (PV) scenarios. Lower left panel (C): mean evaporative fraction, latent heat flux (L) divided by the sum of latent and sensible (H) heat flux (L/(H+H)). Lower right panel (D): accumulated differential energy flux in GigaJoules per square meter. R_{SD} is down-welling short-wave radiation incident on the surface, R_{LD} is down-welling long-wave radiation incident on the surface.

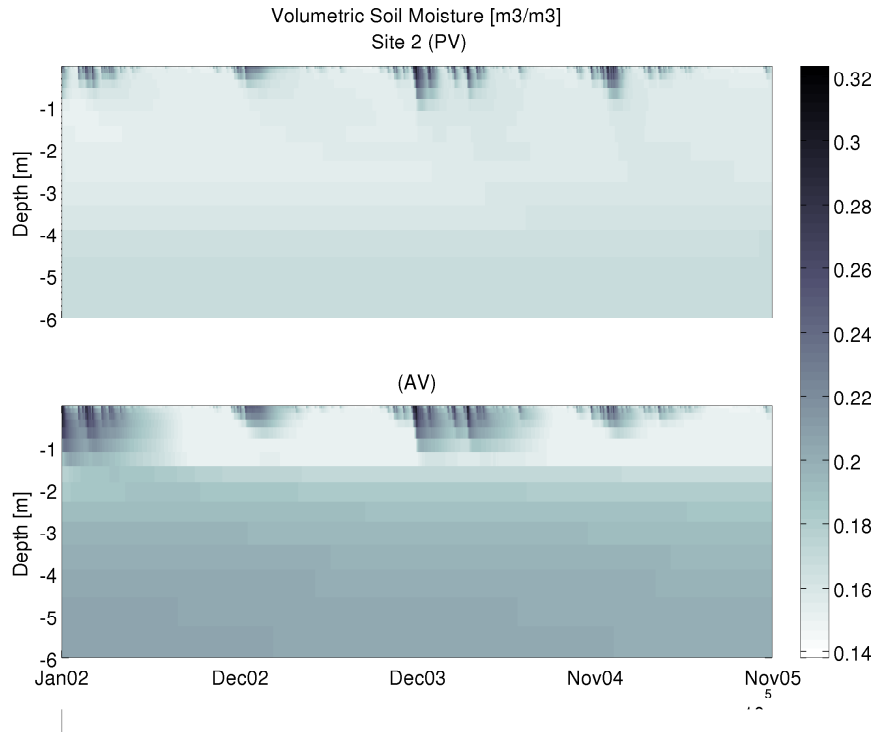

Fig. 010. Time series profile of volumetric soil water at the Gran Chaco focus area. Both scenarios, *Potential* (PV) and *Actual* (AV) are shown separately.

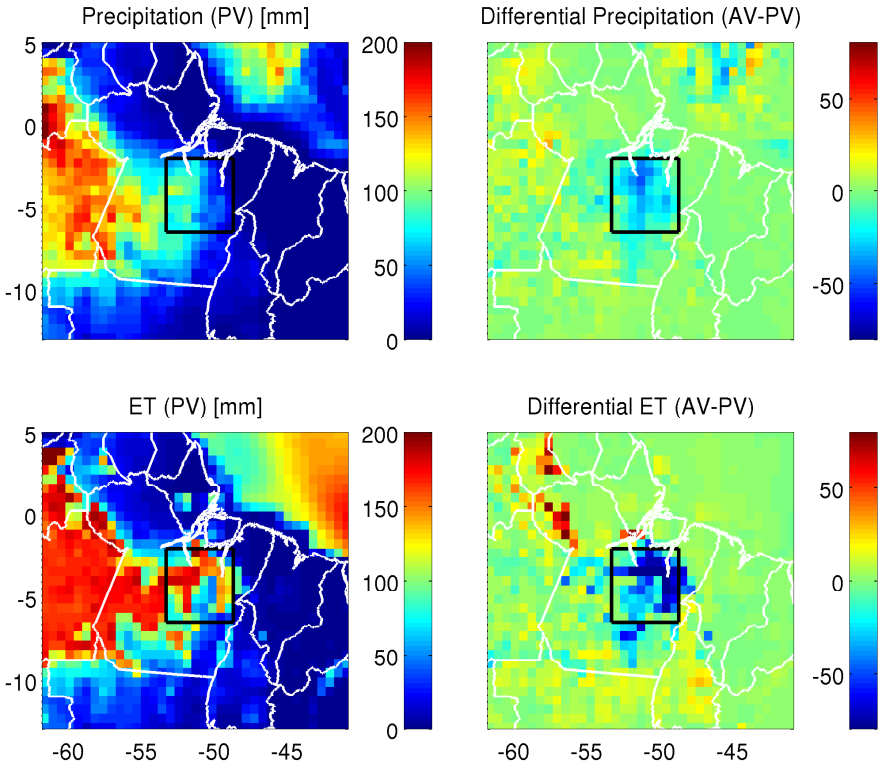

Fig. 011. Monthly integrated hydrologic flux over the Pará focus region, September 2003. Upper left panel: map of integrated monthly precipitation for the *Potential* vegetation simulation (PV). Upper right panel: map of the integrated difference in monthly precipitation, *Actual* vegetation case minus the *Potential* vegetation case (AV-PV). Lower left panel: map of integrated monthly evapotranspiration for the *Potential* vegetation simulation. Lower right panel: map of the integrated difference in monthly evapotranspiration, *Actual* vegetation case minus the *Potential* vegetation case.

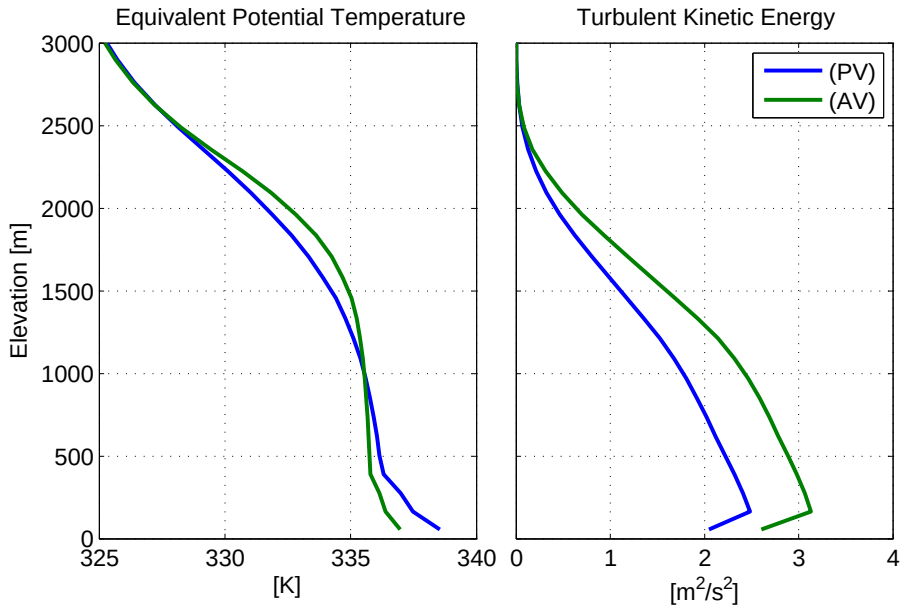

Fig. 012. Mean profiles of Equivalent Potential Temperature and Turbulent Kinetic Energy at 15Z within the bounded domain at Pará, September 2003.

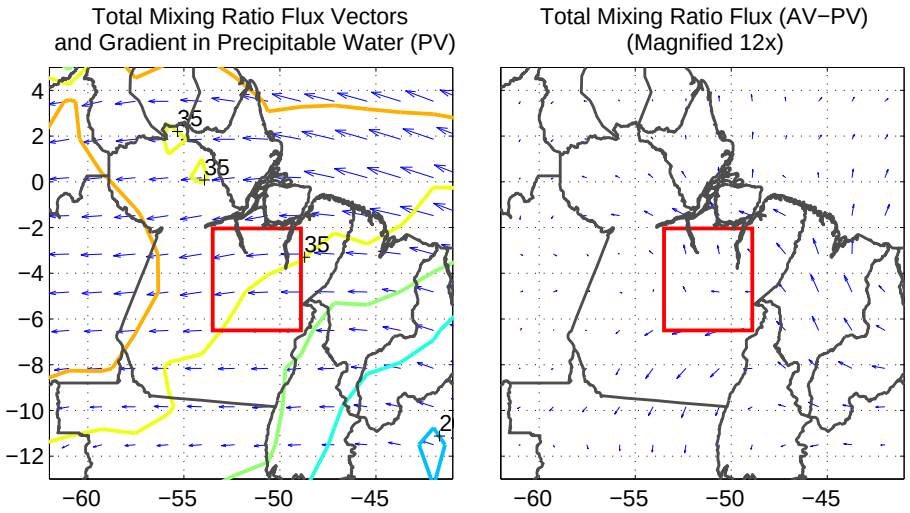

Fig. 013. Left Panel: Map of vertically integrated total water advective flux vectors (quivers) and vertically integrated precipitable water (contours) for the *Potential* vegetation case (PV). September 2003. Quivers are scaled and convey only directionality and relative magnitude. Contours of low precipitable water are shown by cool colors (blues) and high precipitable water with warm colors (reds). Right Panel: The differential in vertically integrated advection of total precipitable water, *Actual* vegetation minus *Potential* vegetation (AV-PV). Quivers are scaled to 12 times relative to the left panel. In both panels the sub-domain bounding the Pará focus region is shown with a red-box.

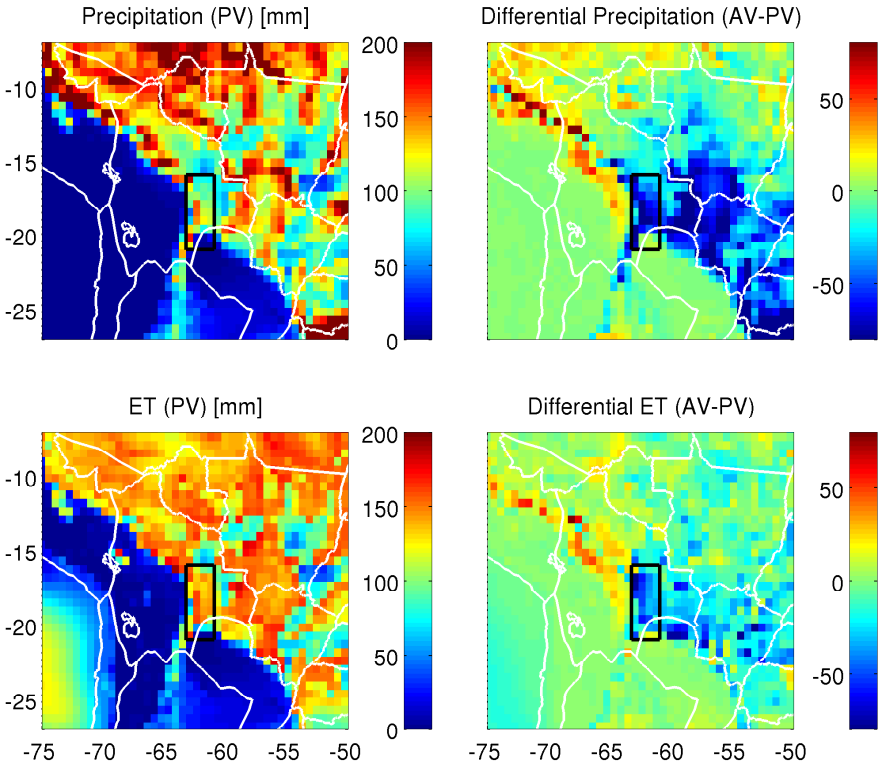

Fig. 014. Monthly integrated surface water fluxes over the Gran Chaco focus region, April 2003. Upper left panel: map of integrated monthly precipitation for the *Potential* vegetation simulation (PV). Upper right panel: map of the integrated difference in monthly precipitation, *Actual* vegetation case minus the *Potential* vegetation case (AV-PV). Lower left panel: map of integrated monthly evapotranspiration for the *Potential* vegetation simulation. Lower right panel: map of the integrated difference in monthly evapotranspiration, *Actual* vegetation case minus the *Potential* vegetation case.

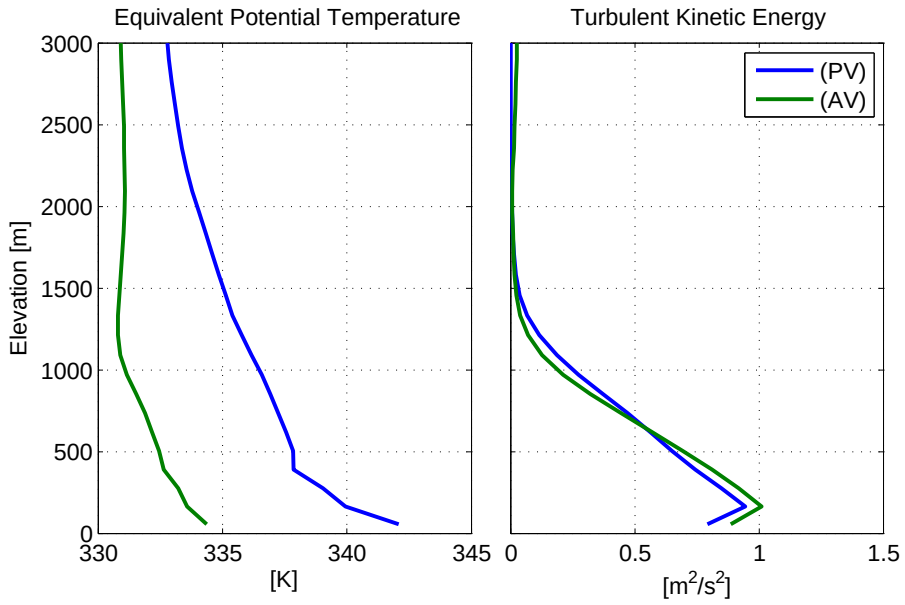

Fig. 015. Mean profiles of Equivalent Potential Temperature and Turbulent Kinetic Energy at 15Z within the bounded domain at Gran Chaco, April 2003.

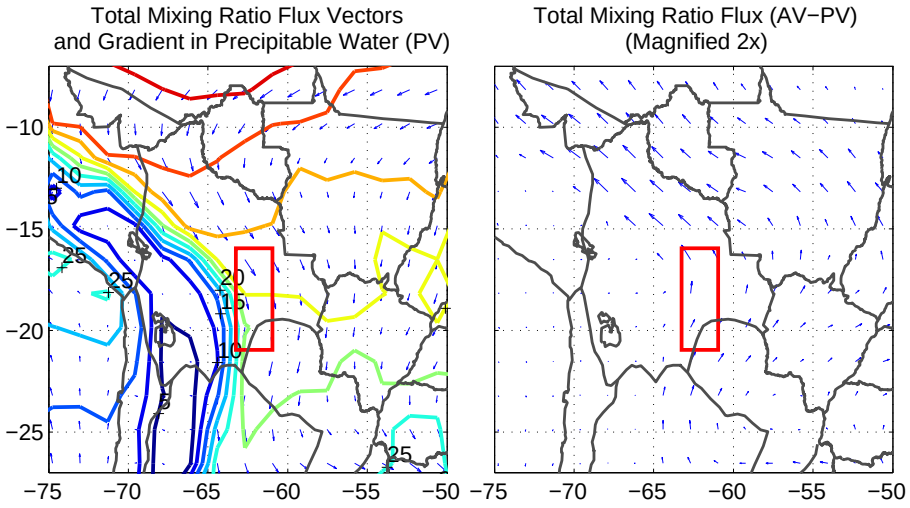

Fig. 016. Left Panel: Map of vertically integrated total water advective flux vectors (quivers) and vertically integrated precipitable water (contours) for the *Potential* vegetation case (PV). September 2003. Quivers are scaled and convey only directionality and relative magnitude. Contours of low precipitable water are shown by cool colors (blues) and high precipitable water with warm colors (reds). Right Panel: The differential in vertically integrated advection of total precipitable water, *Actual* vegetation minus *Potential* vegetation (AV-PV). Quivers are scaled to 2 times relative to the left panel. In both panels the sub-domain bounding the Gran Chaco focus region is shown with a red-box.

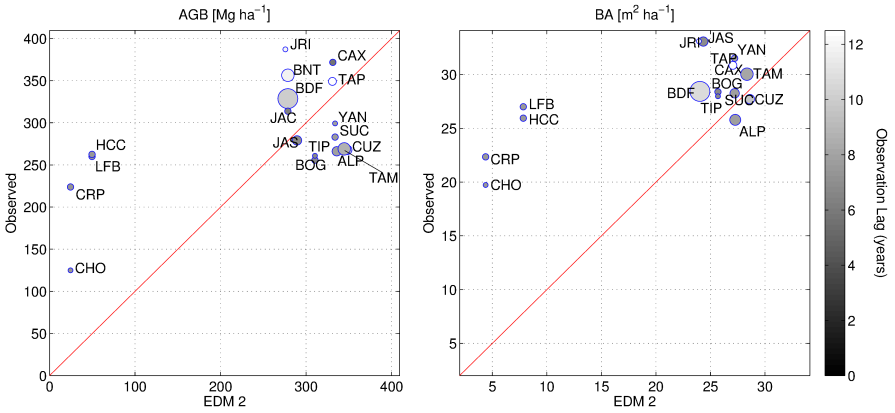

Fig. 017. Comparison of model estimated mean Above Ground Biomass (AGB) and Basal Area (BA) with measurements presented in (Baker et al., 2004a) and (Baker et al., 2004b) Circle size shows relative approximation of the number of census sites used in the field measurements reported in Baker (maximum=11 separate plots at BDF). Darker circles indicate that measurements were taken more recently and therefore have less time-lag in the comparison with the ED2 initial condition (January 2008). In accord with methods of (Baker et al., 2004a) and (Baker et al., 2004b), model estimates were filtered to include only primary forests and ignored vegetation less than 10 centimeters diameter. Coarse woody debris was excluded from comparison, only live stems were accounted for.

Table 01. Simulation constraints describing the spin-up process creating the initial boundary conditions. [1] Modified DS314 data is derived from (Sheffield et al., 2006), precipitation downscaling and radiation interpolation is applied, see footnote for data availability.

Specification	Value
climate data	modified DS314[1]
soils data	(Quesada et al., 2011) + IGBP-DIS
plant types	late succession tropical evergreens mid succession tropical evergreens early succession tropical evergreens subtropical grasses C4 grasses
simulation period	508 years
spatial resolution	gridded 1^o
bounding domain	30^oS-15^oN, 85^oW-30^oW
tree allometry (DBH,height) (crown properties)	 (Chave et al., 2001)(Baker et al., 2004b) (Poorter et al., 2006)(Dietze et al., 2008)
turbulent transport	(Beljaars and Holtslag, 1991) atmospheric boundary (Massman, 1997) within canopy
photosynthesis & leaf conductance	(Collatz et al., 1991) (Collatz et al., 1992) (Leuning, 1995)
canopy radiation scattering	(Zhao and Qualls, 2005),(Zhao and Qualls, 2006)
soil hydrology	(Walko et al., 2000),(Tremback and Kessler, 1985) (Medvigy et al., 2009)

Table 02. Run time parameters and specifications in the ED2-BRAMS coupled simulations. [1] LFC = Level of Free Convection.

Specification	Value
simulation period	January 2002 - December 2005
grid projection	polar stereographic
grid dimensions	98 (E-W), 86 (N-S), 56 (vertical)
horizontal grid resolution	64 km
vertical grid resolution	110 m (lowest) stretching to 1500 m at 7%
atmospheric time-step	30 s
atmospheric accoustic time-step	10 s
land-surface model time-step	120 s
method of calculating updraft base	level of maximum sum of mean and variance of vertical velocity
number of prototype cloud scales	2
mean radius of cloud 1	20,000 m
minimum depth of cloud 1	4000 m
mean radius of cloud 2	800 m
minimum depth of cloud 2	80 m
cumulus convective scheme	(Grell and Dévényi, 2002)
cumulus convective trigger	pressure differential between updraft base and LFC[1] < 100 hpa
cumulus dynamic control	(Kain and Fritsch, 1990),(Kain, 2004)
condensate to precipitation conversion efficiency	3%
cloud # concentrations and distribution parameters	(Medvigy et al., 2010)
turbulent closure	(Nakanishi and Niino, 2006)
short-wave radiation scattering	(Harrington and Olsson, 2001)
long-wave radiation scattering	(Chen and Cotton, 1983)
advection	monotonic, (Walcek and Aleksic, 1998) & (Freitas et al., 2012)
cumulus feedback on radiation?	Yes

Table 03. Hydrologic monthly means within the bounded area above case study 1, September 2003. Total change in column precipitable water for the month per square meter ΔM_{pw}, evapotranspiration ET, precipitation P and resolved moisture convergence Mc, 55 meter air temperature T, mixing ration (55m) r, equivalent potential temperature θ_e, surface albedo to short-wave radiation α, down-welling short-wave radiation R_{SD}, down-welling long-wave radiation R_{LD}, up-welling long-wave radiation R_{LU}, net surface radiation R_{net}, sensible heat flux SHF and latent heat flux LHF.

Case	ΔM_{pw}	ET	P	Mc	T	r
Units	$\mathrm{kg\,m^{-2}}$	$\mathrm{kg\,m^{-2}}$	$\mathrm{kg\,m^{-2}}$	$\mathrm{kg\,m^{-2}}$	$^{\circ}\mathrm{C}$	$\mathrm{g\,kg^{-1}}$
AV	-3.457	63.1	29.8	-37.14	32.83	12.18
PV	-3.515	94.7	47.3	-51.32	32.35	12.93

Case	θ_e	α	R_{SD}	R_{LD}	R_{LU}	R_{net}	SHF	LHF
Units	K	-	$\mathrm{W\,m^{-2}}$	$\mathrm{W\,m^{-2}}$	$\mathrm{W\,m^{-2}}$	$\mathrm{W\,m^{-2}}$	$\mathrm{W\,m^{-2}}$	$\mathrm{W\,m^{-2}}$
AV	336.8	0.262	300.2	443.3	513.2	180.9	139.25	70.97
PV	338.2	0.257	285.6	443.9	498.0	187.8	114.50	106.45

Table 04. Hydrologic monthly means within the bounded area above the Gran Chaco case study, April 2003. Total change in column precipitable water for the month per square meter ΔM_{pw}, evapotranspiration ET, precipitation P and resolved moisture convergence Mc, 55 meter air temperature T, mixing ration (55m) r, equivalent potential temperature θ_e, surface albedo to short-wave radiation α, down-welling short-wave radiation R_{SD}, down-welling long-wave radiation R_{LD}, up-welling long-wave radiation R_{LU}, net surface radiation R_{net}, sensible heat flux SHF and latent heat flux LHF.

Case	ΔM_{pw}	ET	P	Mc	T	r
Units	$\mathrm{kg\,m^{-2}}$	$\mathrm{kg\,m^{-2}}$	$\mathrm{kg\,m^{-2}}$	$\mathrm{kg\,m^{-2}}$	$^{\circ}\mathrm{C}$	$\mathrm{g\,kg^{-1}}$
AV	-11.42	82.95	41.89	-52.49	25.98	12.73
PV	-11.02	111.89	85.91	-36.99	27.36	15.15

Case	θ_e	α	R_{SD}	R_{LD}	R_{LU}	R_{net}	SHF	LHF
Units	K	-	$\mathrm{W\,m^{-2}}$	$\mathrm{W\,m^{-2}}$	$\mathrm{W\,m^{-2}}$	$\mathrm{W\,m^{-2}}$	$\mathrm{W\,m^{-2}}$	$\mathrm{W\,m^{-2}}$
AV	334.4	0.330	252.6	400.2	466.9	111.74	38.54	91.0
PV	342.0	0.297	218.7	424.9	462.6	130.2	28.15	122.5

Table 05. Atmospheric boundary conditions provided by BRAMS, that drive the ED2 model.

Symbol	Units	Description
u_x	$[m/s]$	Zonal wind speed
u_y	$[m/s]$	Meridional wind speed
T_a	$[K]$	Air temperature
q_a	$[kg/kg]$	Air specific humidity
$\dot{m}_{pcp}$	$[kg/s]$	Precipitation mass rate
z_{ref}	$[m]$	Height of the reference point
R_{ld}	$[w/m^2]$	Downward longwave radiation
R_{vb}	$[w/m^2]$	Downward shortwave radiation, visible beam
R_{vd}	$[w/m^2]$	Downward shortwave radiation, visible diffuse
R_{nb}	$[w/m^2]$	Downward shortwave radiation, near infrared beam
R_{nd}	$[w/m^2]$	Downward shortwave radiation, near infrared diffuse

Table 06. ED2 flux variables providing the lower boundary condition for the BRAMS atmospheric model.

Symbol	Units	Description
$\overline{(u'w')}$	$[m^2/s^2]$	Average vertical flux of horizontal wind velocity perturbations
$\overline{(w'w')}$	$[m^2/s^2]$	Average vertical flux of vertical wind velocity perturbations
$\overline{(t'w')}$	$[mK/s^2]$	Average vertical flux of temperature perturbations
$\overline{(q'w')}$	$[kg/m^2/s^2]$	Average vertical flux of moisture perturbations
$\overline{(c'w')}$	$[\mu mol/m^2/s^2]$	Average vertical flux of carbon perturbations
χ_s	[-]	Average total shortwave albedo
χ_l	[-]	Average total longwave albedo
R_{lu}	$[w/m^2]$	Average up-welling longwave radiation

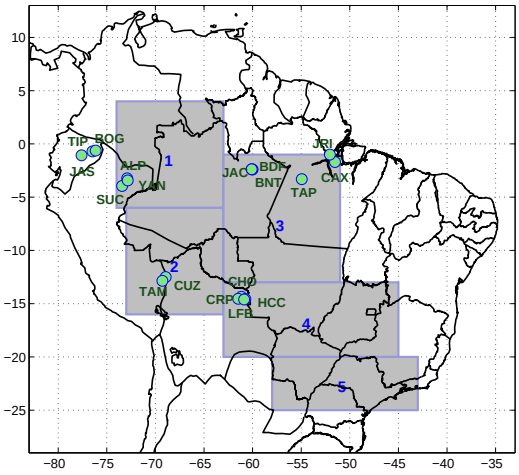

Fig. 018. Locations of zones and sites of analysis. Zones are numbered 1 through 5, and reflect geographic areas where model and observation spatial means are compared for validation (see Appendix). Forest census plot sites from (Baker et al., 2004a) and (Baker et al., 2004b) are referenced with green markers and their station code. Station codes designate the following site names: Allpahuayo (ALP), BDFFP (BDF), Bionte (BNT), Bogi (BOG), Caxiuana (CAX), Chore (CHO), Cerro Pelao (CRP), Cuzco Amazonico (CUZ), Huanchaca Dos (HCC), Jacaranda (JAC), Jatun Sacha (JAS), Jari (JRI), Los Fierros Bosque (LFB), Sucusari (SUC), Tambopata (TAM), Tapajos (TAP), Tiputini (TIP) and Yanamono (YAM).

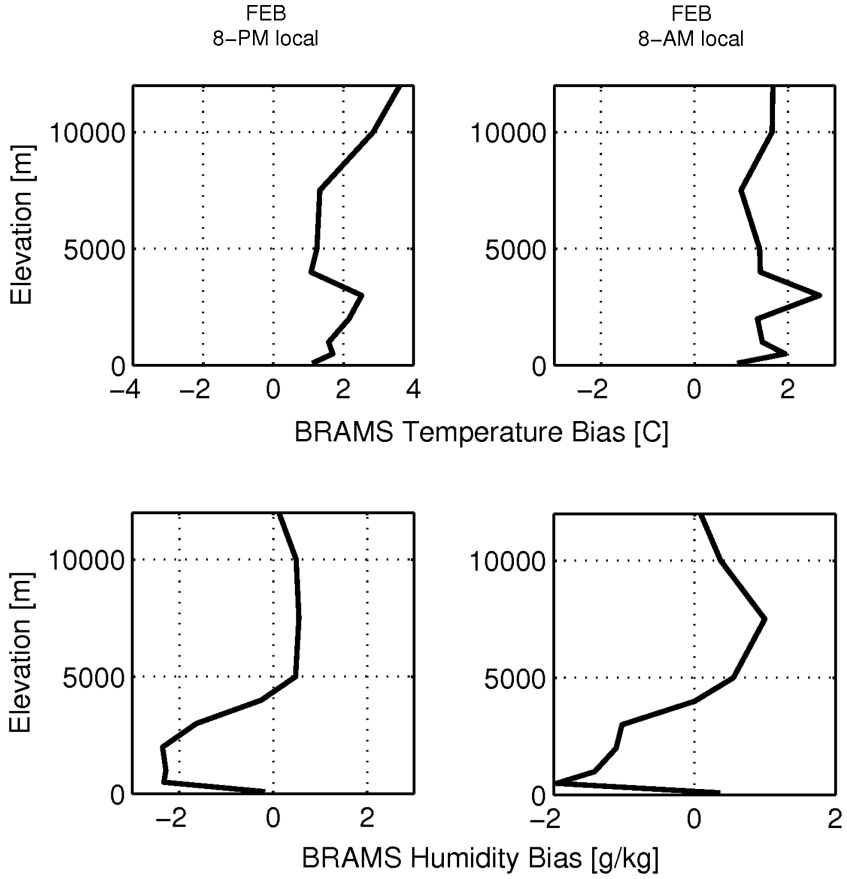

Fig. 019. Comparison of model estimates with radiosonde data, differences in mean air temperature and specific humidity. Manaus, February 2003.

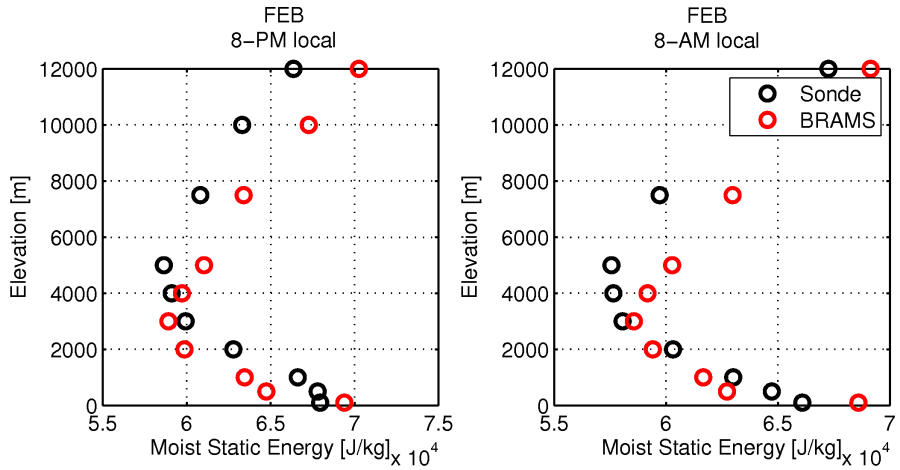

Fig. 020. Comparison of model estimates with radiosonde data, mean wind magnitude and mean moist static energy. Manaus, February 2003.

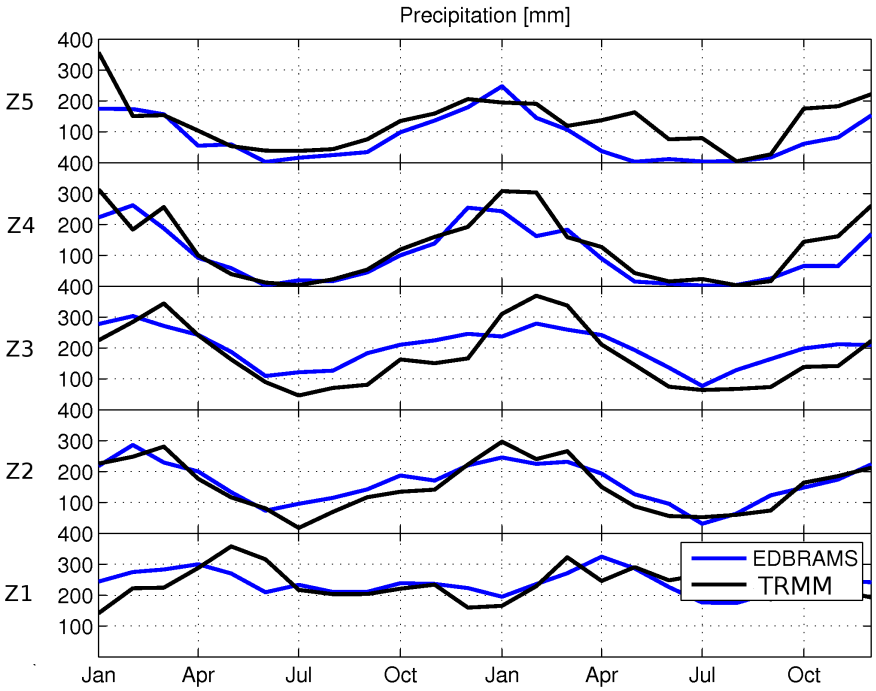

Fig. 021. Mean monthly precipitation from ED2-BRAMS and the Tropical Rainfall Measurement Mission (TRMM) 3B43 product, years 2002-2003. Spatial means are taken within zones according to Figure 018.

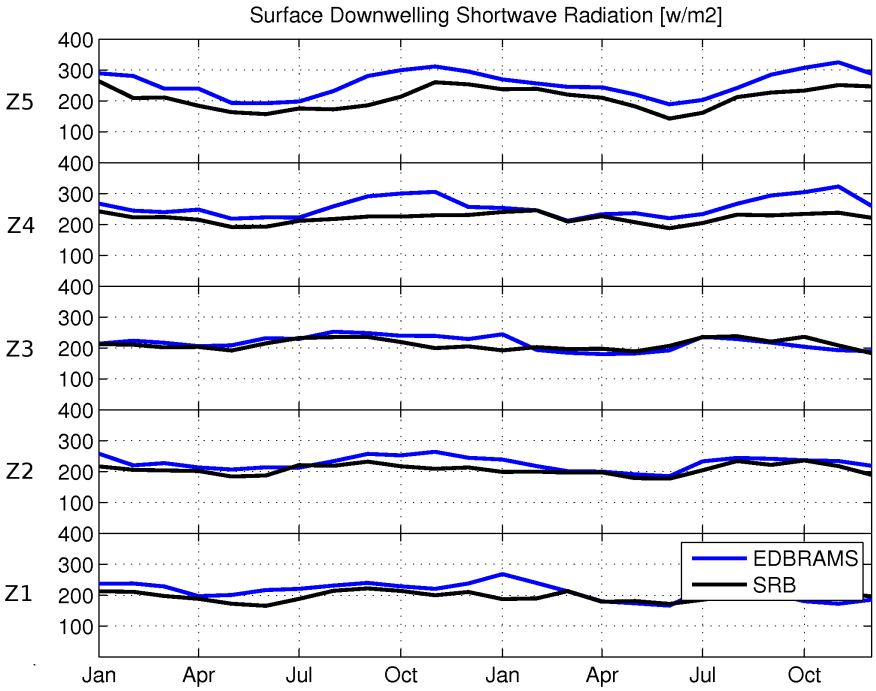

Fig. 022. Mean monthly surface radiation from ED2-BRAMS and the Surface Radiation Budget (SRB) product, years 2002-2003. Spatial means are taken within zones according to Figure 018.

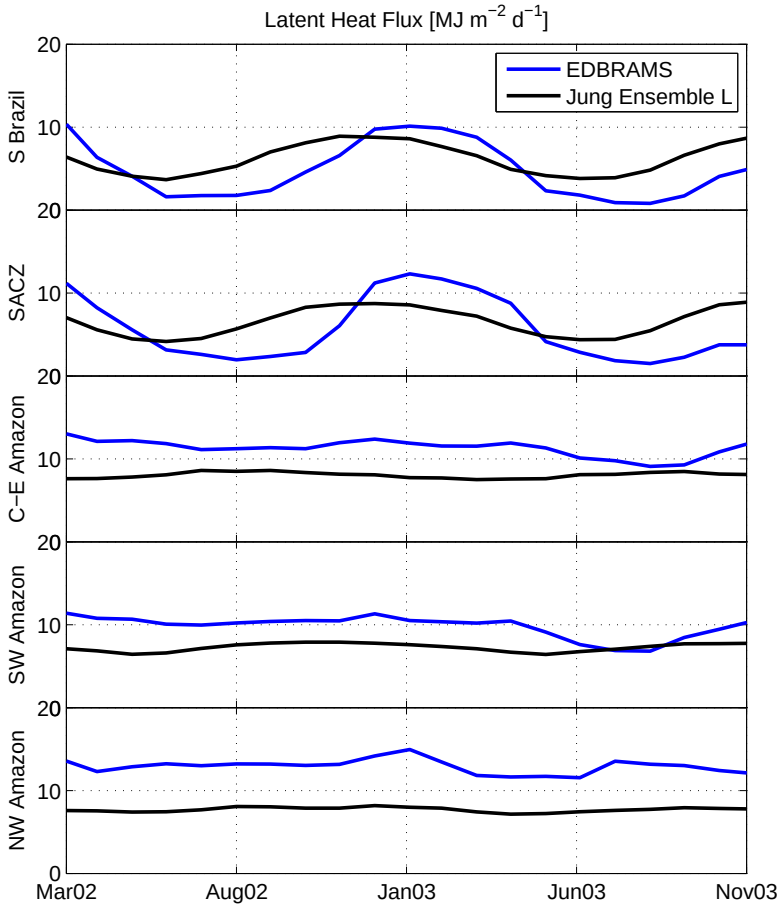

Fig. 023. Mean monthly surface to atmosphere latent heat flux from ED2-BRAMS and the synthesis product from (Jung et al., 2011)(Jung et al., 2009). Spatial means are calculated over the zones shown in Figure 018.

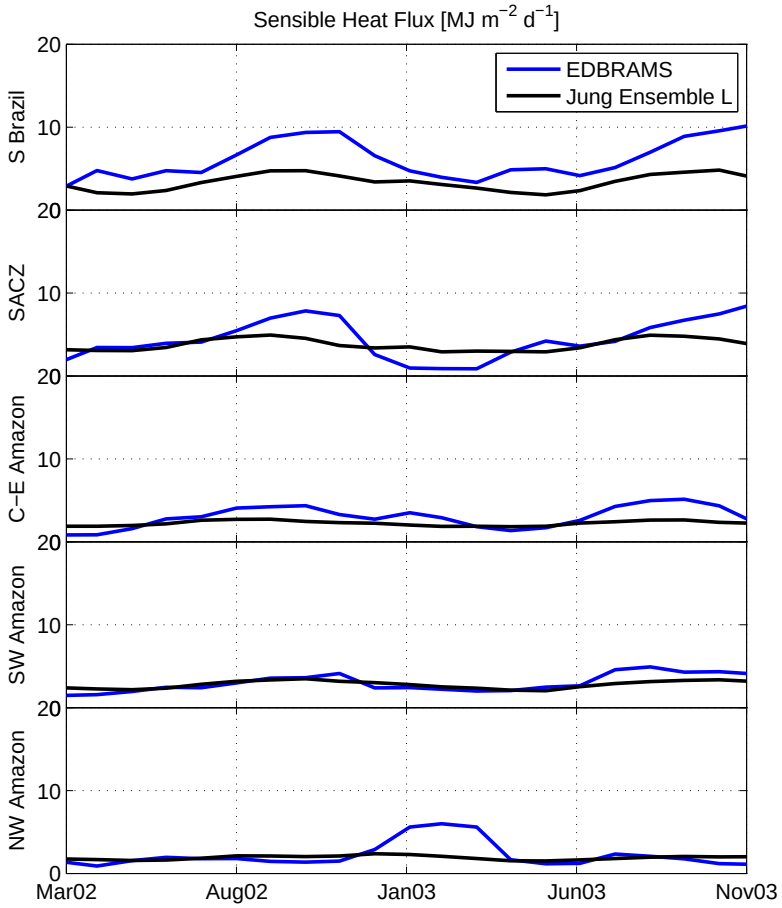

Fig. 024. Mean monthly surface to atmosphere sensible heat flux from ED2-BRAMS and the synthesis product from (Jung et al., 2011)(Jung et al., 2009). Spatial means are calculated over the zones shown in Figure 018.

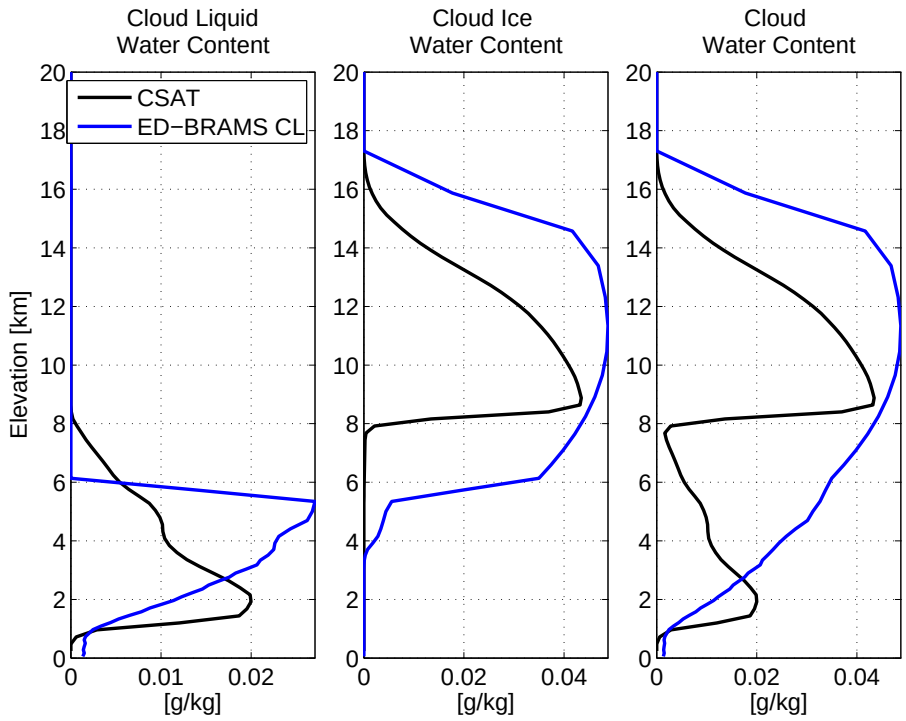

Fig. 025. CloudSat climatological water content profiles and model estimated water content profiles for February 2003, 17 UTC, $3^oN - 12^oS$ and $70^oW - 55^oW$.